



## Thermocapillary instability for a shear-imposed falling film

Arnab Choudhury  and Arghya Samanta <sup>\*</sup>*Department of Applied Mechanics, Indian Institute of Technology Delhi, 110016 Delhi, India*

(Received 3 February 2023; accepted 12 September 2023; published 27 September 2023)

We investigate the linear stability analysis of a gravity-driven three-dimensional incompressible viscous fluid flowing down a uniformly heated inclined plane under the influence of an external constant shear stress on the fluid surface. Based on a coupled system of boundary value problems involving the amplitudes of the perturbation normal velocity and perturbation temperature, the stability analysis is accomplished for infinitesimal disturbances of arbitrary wave numbers. The analytical solution of the boundary value problems in the long-wave regime reveals the existence of the H-mode, which is destabilized by both the Marangoni number and the imposed shear stress acting in the coflow direction. Furthermore, we determine the critical value of the Marangoni number below which the inertialess flow is linearly stable, but the flow may be linearly unstable in this range due to inertia. However, the numerical solution based on the Chebyshev spectral collocation method reveals the existence of additional thermocapillary S-mode and thermocapillary P-mode in the long-wave and finite streamwise wave number regimes, respectively. It is found that the H-mode and S-mode instabilities are destabilized, but the P-mode instability is stabilized if the constant shear stress is applied in the coflow direction. Interestingly, as the imposed shear stress rises, the onset of instability for the H-mode and the onset of stability for the S-mode merge with each other and produce a single onset for the primary stability. However, a completely opposite phenomenon takes place if a constant shear stress is imposed in the counterflow direction. In addition, we observe that the shear mode exists in the high Reynolds number regime, and the associated instability can be initiated at a lower Reynolds number by applying a constant shear stress in the coflow direction. Conversely, the shear mode instability can be delayed by imposing a constant shear stress in the counterflow direction. Finally, the spanwise wave number exhibits a stabilizing influence on the H-mode, S-mode, and shear mode instabilities but exhibits a destabilizing influence on the P-mode instability.

DOI: [10.1103/PhysRevFluids.8.094006](https://doi.org/10.1103/PhysRevFluids.8.094006)

### I. INTRODUCTION

During the past few decades, the subject of interfacial heat transfer and the stability of thin liquid films has become attractive in engineering and science due to their immense applications. Because of their large contact area and low thermal resistance, thin films are frequently used in several industrial equipment, such as falling film evaporator, condenser, etc. [1]. Frisk and Davis [2] and Brauner and Maron [3] reported that surface wave formation significantly enlarges the rate of heat and mass transfers on the film surface and, consequently, plays a crucial role in the surface wave dynamics and their transition to spatio-temporal chaos. Furthermore, thin films are very useful things for the thermal protection of rocket engines and the cooling of micro-electronic devices. In addition, the studies of thin films have huge importance in the coating industry for the quality of surface coating. For the above reasons, we are motivated to conduct the present study.

---

<sup>\*</sup>arghya@am.iitd.ac.in

In this context, Kapitza and Kapitza [4] pioneered the experimental study of isothermal falling film in the moderate Reynolds number regime. They observed the formation of a large tear-drop-shape solitary wave on the surface of a falling film far away from the inception zone. Later, the theoretical studies of the isothermal film flowing down an inclined plane were initiated by Benjamin [5] and Yih [6] in the low Reynolds number regime. They essentially performed the linear stability analysis and determined the critical Reynolds number for the onset of the H-mode/surface mode instability analytically. After that, Lin [7], Bruin [8], and Chin *et al.* [9] predicted the existence of shear mode in the high Reynolds number regime. However, they did notice that the inclination angle should be sufficiently small to allow the shear mode to emerge. As discussed by Bruin, the surface mode and the shear mode compete with each other to trigger the primary instability in the zone of low inclination angle. Floryan *et al.* [10] further conducted the above study to take into account the influence of surface tension on the shear mode. The following papers (Alekseenko *et al.* [11], Chang [12], Liu and Gollub [13], Oron *et al.* [14], Craster and Matar [15]) are very relevant to researchers in understanding the dynamics of falling films.

In parallel, the linear stability analysis of a nonisothermal liquid film flowing down a heated inclined plane was originated by Lin [16] in the low Reynolds number regime. Using the long-wave analysis, he calculated the critical Reynolds number analytically for the onset of H-mode instability. Later, the above study was further revisited by Sreenivasan and Lin [17] to assess the thermocapillary instability in the arbitrary wave number regime. In the long-wave regime, the role of the Prandtl number in the thermocapillary instability was examined by Smith [18]. As reported by Smith, the base flow can be susceptible to instability due to the infinitesimal perturbation at higher values of the Prandtl number. His study also deciphered the physical mechanism for the initiation of linear instability. An alternative physical mechanism of instability for the falling film over a uniformly heated substrate was provided by Goussis and Kelly [19,20] through the method of energy budget. In their studies, the hydrodynamic mode (H-mode) and the thermocapillary modes (S-mode and P-mode) were identified in low to moderate Reynolds number regimes. As discussed by them, there exist two distinct physical mechanisms for generating the destabilizing thermocapillary forces responsible for the S-mode and P-mode instabilities. In particular, the thermocapillary S-mode instability arises from the modification of the basic temperature due to the deformation of the fluid surface. It generally occurs in the long-wave regime. However, the thermocapillary P-mode instability arises from the convective interaction between the perturbation velocity field and the basic temperature. This P-mode instability occurs in the finite wave number regime. Moreover, they reported that the following criterion should be satisfied for the appearance of P-mode instability in a viscous fluid layer [19,20],

$$\left[ -\frac{d\sigma}{dT} \Delta T \right] \frac{\rho c_p}{\mu \lambda} > 32.073, \quad (1)$$

where  $\sigma$  is the surface tension,  $\Delta T$  is the difference between the wall temperature and the ambient temperature,  $\rho$  is the density,  $c_p$  is the specific heat capacity at constant pressure,  $\mu$  is the dynamic viscosity, and  $\lambda$  is the heat transfer coefficient at the fluid surface. Indeed, the expression  $[-\frac{d\sigma}{dT} \Delta T]$  is a measure of the thermocapillary force generated due to the change in surface tension caused by the temperature variation, while the expression  $\rho c_p$  is a measure of the effect of convection in extracting energy from the basic state. Obviously, the large magnitudes of these quantities support the appearance of P-mode instability. As the dynamic viscosity  $\mu$  and the heat transfer coefficient  $\lambda$  are, respectively, measures of the energy loss due to viscous dissipation and of the heat loss through the fluid surface, these two quantities oppose the P-mode instability. Hence, for the appearance of P-mode instability, the energy transfer from the basic state to the disturbance and the work done by the thermocapillary force should be greater than these kinds of energy losses. Furthermore, Goussis and Kelly showed that the H-, S-, and P-modes are destabilized by the Marangoni number. The effect of evaporation on thermocapillary instability was introduced by Joo *et al.* [21]. They also performed a linear stability analysis based on the long-wave asymptotic expansion. To explore the

nonlinear stability induced by the H-mode, Joo *et al.* [22] further revisited their previous study. As a result, the evolution equation was developed in terms of the liquid film thickness. Their result predicted that the rivulet on the film surface forms due to the thermocapillary S-mode instability. After that, a complete study on the falling film instability over a heated substrate was accomplished by Ruyer-Quil *et al.* [23] and Scheid *et al.* [24]. In their studies, a low-dimensional model in terms of the local film thickness, local flow rate, and mean temperature across the film layer was developed. Both linear and nonlinear stability analyses were performed. Their results showed a very good match with the results obtained from the Orr-Sommerfeld boundary value problem. Furthermore, the hydrodynamic mode (H-mode) and the thermocapillary mode (S-mode) were recognized in their numerical simulation. As discussed by them, the H-mode and the S-mode instabilities reinforce each other as the Marangoni number increases. In the case of the nonisothermal binary liquid film, Hu *et al.* [25] carried out the study of absolute and convective instabilities. The hydrodynamic mode (H-mode) and the thermocapillary modes (S-mode and P-mode) were identified in their study. They demonstrated that the unstable modes are destabilized by the Soret number, as was observed for the Marangoni number. In addition, they showed that the H-mode and the S-mode coalesce with each other as the Soret number rises. The above study was further revisited by Pascal and D'Alessio [26] and D'Alessio and Pascal [27] under the framework of the Orr-Sommerfeld-type and depth-averaged equations, respectively. They carried out the linear and nonlinear stability analyses. Samanta [28] examined the temporal inertialess instability of a liquid film flowing over a uniformly heated substrate. The destabilizing effect of the Biot number on the temporal mode was reported. Dávalos-Orozco [29] executed a nonlinear stability analysis for the heated liquid film by using the Benney-type surface evolution equation. His intention was to investigate the effects of wall thickness and heat conductivity on the unstable modes. A review of the isothermal and nonisothermal falling liquid films can be found in the work of Dávalos-Orozco [30]. The study on the instability of a liquid film flowing over a uniformly heated slippery substrate was conducted by Ding and Wong [31]. They calculated the critical Reynolds number analytically for the onset of H-mode instability. The Benney-type surface evolution equation and the weighted residual three-equation model were developed for the instability analysis. As shown by them, the Benney-type surface evolution equation provided a good result only close to the threshold of instability. However, the weighted residual three-equation model supplied a good result up to a moderate value of the Reynolds number. Their results also revealed that the amplitude of the traveling wave amplifies as the slip length increases. The linear stability analysis of a binary liquid film flowing down a heated slippery substrate was explored by Ellaban *et al.* [32] in the low Reynolds number zone. They predicted that both the slip length and the Marangoni number have a destabilizing influence on the H-mode and S-mode instabilities. The instability of gravity-driven films flowing over a heated porous substrate was analyzed by Thiele *et al.* [33], Sadiq *et al.* [34], and Ogden *et al.* [35]. In all these studies, it was reported that permeability has a destabilizing influence on the H-mode instability. Recently, Choudhury and Samanta [36] accomplished a detailed study on the thermocapillary instability of a liquid film flowing over a slippery plane. They found an additional shear mode in the high Reynolds number regime. Their results revealed that the thermocapillary P-mode is destabilized by the wall slip. But the shear mode instability becomes weaker with increasing value of the slip length. Furthermore, the thermocapillary P-mode instability becomes stronger as the spanwise wave number increases. However, the investigation of the spreading front of a free surface profile of a viscous film that is released onto a sloping surface was initiated by Huppert [37] based on the lubrication approximation, where the effect of the contact line was neglected. He demonstrated that the wavelength of the fingering front is dependent on the surface tension but independent of the coefficient of viscosity. Later, this study was further explored by Troian *et al.* [38] by including the motion of the contact line. As discussed by them, the advancing film front can be unstable to fingers in the perpendicular direction of the main flow, where the surface tension force is comparable to the forces due to viscosity and gravitational acceleration. Furthermore, they reported that this fingering instability is completely unrelated to the H-mode instability deciphered in the present study. After that, the above flow problem was further revisited by Cazabat *et al.* [39] and Kataoka and Troian [40]

to examine the fingering instability at the advancing film front caused by the Marangoni effect. As the variation of surface tension with temperature is fairly constant for many fluids, they imposed a constant temperature gradient along the impermeable substrate to generate a constant surface tension gradient, or equivalently, a constant Marangoni surface stress along the direction of the flow, that forces the liquid film to spread in the direction of the higher surface tension zone [39]. Two different regimes were recognized: an outer region far from the leading edge where the Marangoni force balances the viscous force, and an inner region near the leading edge where the capillary force is also significant along with the viscous and Marangoni forces. Although the aim of the present study is to explore the hydrodynamic instabilities induced by the H-mode, S-mode, P-mode, and shear mode, we have further tried to relate our present study to the spreading front problem of a viscous film, where the applied constant shear stress generated by the air flow across the film surface behaves like the constant Marangoni surface stress created by the constant temperature gradient proposed in the previous study [41]. The discussion can be found in Appendix E.

In the context of a shear-imposed flow, Smith [42] first rendered a physical mechanism of instability for the H-mode/surface mode, where a constant shear stress is applied at the surface of a gravity-driven falling film. He performed a linear stability analysis in the long-wave regime. After that, Wei [43] studied the same problem, but the insoluble surfactant was introduced at the film surface. As a result, the surfactant mode emerges along with the H-mode. He reported that the imposed shear stress destabilizes the H-mode in the long-wave regime. Later, Samanta [44] extended the study of Smith in the moderate Reynolds number regime. Both linear and nonlinear stability analyses were carried out based on the low-dimensional model involving the local film thickness and the local flow rate. According to Samanta, the H-mode instability begins as soon as the kinematic wave speed exceeds the speed of the dynamic wave. Furthermore, it was demonstrated that the amplitude of the traveling wave amplifies if the constant shear stress is imposed in the coflow direction. Bhat and Samanta [45] further revisited the same problem to decipher the shear mode, which generally appears in the finite wave number regime when the Reynolds number is very large. As discussed by them, the shear mode can be destabilized by incorporating a constant shear stress in the coflow direction. Recently, Samanta [46] executed the spatio-temporal analysis for the shear-imposed film flow. It was demonstrated that the H-mode is convectively unstable. Trifonov [47,48] and Tselodub and Bocharov [49,50] investigated the two-phase gas-liquid flows, where the upper phase is taken as a laminar gas flow. Consequently, the Navier-Stokes equations were employed to govern the flows for both liquid and gas phases.

The above literature survey reveals that most of the studies on thermocapillary instability are two-dimensional, and there is no investigation of the spanwise wave number in the most unstable modes. Furthermore, there is no study on the effect of imposed shear stress on the thermocapillary instability. For these reasons, we are interested in exploring the thermocapillary instability of a shear-imposed film flowing down an inclined plane when a constant shear stress is applied either in the coflow direction or in the counterflow direction. In the present study, our concern is to decipher the impact of imposed shear stress on the individual modes, such as H-mode, S-mode, P-mode, and shear mode. The paper is organized as follows: The mathematical formulation is provided in Sec. II. The analytical solution of the Orr-Sommerfeld-type boundary value problems is rendered in Sec. III, while the numerical simulation of the Orr-Sommerfeld-type boundary value problems can be found in Sec. IV. Results in low to moderate Reynolds number regimes are produced in Sec. V, but the results in the high Reynolds number regime are supplied in Sec. VI. Inertialess stability analysis is investigated in Sec. VII. Inviscid stability analysis is discussed in Sec. VIII. The summary and conclusions are presented in Sec. IX.

## II. MATHEMATICAL FORMULATION

Consider a three-dimensional gravity-driven incompressible viscous fluid flowing down a heated inclined plane in the presence of an imposed shear stress  $\tau_s$  in the streamwise direction ( $x > 0$ ), as sketched in Fig. 1. If  $\tau_s > 0$ , then we say that the shear stress is acting in the coflow direction.

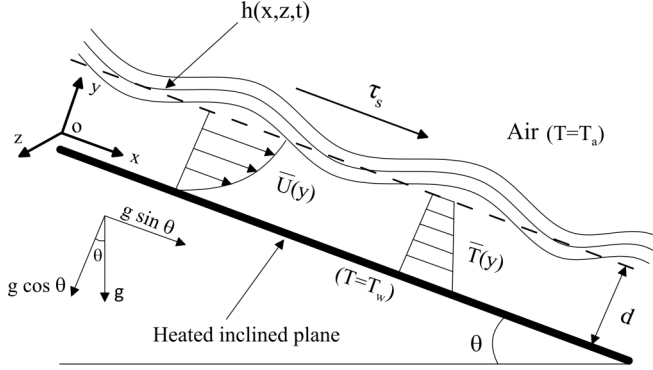


FIG. 1. Sketch of a viscous film flowing down a heated inclined plane in the presence of an imposed shear stress in the streamwise direction. The constant shear stress  $\tau_s$  is acting in the coflow direction if  $\tau_s > 0$ . However, it is acting in the counterflow direction if  $\tau_s < 0$ . Here,  $\bar{U}(y)$  and  $\bar{T}(y)$  represent the base velocity and base temperature profiles, respectively.

Otherwise, if  $\tau_s < 0$ , then the shear stress is acting in the counterflow direction. Here,  $\theta$  is the inclination angle with the horizontal line. We assume that the plane is uniformly heated with a temperature of  $T = T_w$ . Since, our goal is to explore the thermocapillary instability, the density  $\rho$  and the dynamic viscosity  $\mu$  of the fluid are assumed to be constants. However, the surface tension  $\sigma(T)$  of the fluid is not constant but varies linearly with the temperature by the following formula [19]:

$$\sigma(T) = \sigma_a - \gamma(T - T_a), \quad (2)$$

where  $\sigma_a$  is the surface tension of the fluid at the ambient temperature of  $T = T_a$  and  $\gamma = -\frac{d\sigma}{dT}|_{T=T_a} > 0$ , because the surface tension of the fluid decreases as the temperature increases. Suppose the origin of the Cartesian coordinate system lies on the inclined plane, and the axes  $x$ ,  $y$ , and  $z$  are labeled in streamwise, cross-stream, and spanwise flow directions, respectively. The undisturbed fluid layer thickness is  $d$ , which is specified by the dashed straight line, while the disturbed fluid layer thickness is  $h(x, z, t)$ , which is specified by the solid curvy line. The nonisothermal fluid flow is governed by the continuity, momentum, and energy equations [51–53]

$$\partial_x u + \partial_y v + \partial_z w = 0, \quad (3)$$

$$\rho(\partial_t u + u\partial_x u + v\partial_y u + w\partial_z u) = -\partial_x p + \mu(\partial_{xx} u + \partial_{yy} u + \partial_{zz} u) + \rho g \sin \theta, \quad (4)$$

$$\rho(\partial_t v + u\partial_x v + v\partial_y v + w\partial_z v) = -\partial_y p + \mu(\partial_{xx} v + \partial_{yy} v + \partial_{zz} v) - \rho g \cos \theta, \quad (5)$$

$$\rho(\partial_t w + u\partial_x w + v\partial_y w + w\partial_z w) = -\partial_z p + \mu(\partial_{xx} w + \partial_{yy} w + \partial_{zz} w), \quad (6)$$

$$\rho c_p(\partial_t T + u\partial_x T + v\partial_y T + w\partial_z T) = \kappa(\partial_{xx} T + \partial_{yy} T + \partial_{zz} T), \quad (7)$$

where  $u$ ,  $v$ ,  $w$ ,  $p$ , and  $T$  are the velocity components, pressure, and temperature of the fluid, respectively. The notation  $g$  denotes the acceleration due to gravity,  $\kappa$  denotes the thermal conductivity, and  $c_p$  denotes the specific heat capacity at constant pressure. As the temperature varies, the thermal conductivity  $\kappa$  and the specific heat capacity  $c_p$  are assumed to be constants. The boundary conditions are as follows: (i) At the inclined plane,  $y = 0$ , the streamwise, cross-stream, and spanwise velocity components must satisfy the no-slip and no-penetration boundary conditions, respectively, while the temperature on the inclined plane is constant. Hence, we can use [28]

$$u = 0, \quad v = 0, \quad w = 0, \quad T = T_w, \quad \text{at } y = 0, \quad (8)$$

where  $T_w$  is the constant temperature on the plane. (ii) At the fluid surface,  $y = h(x, z, t)$ , the dynamic boundary conditions are obtained by balancing the hydrodynamic stress, the surface stress generated by the surface tension times the curvature of the fluid surface, the Marangoni stress generated by the surface tension gradient due to the change in temperature, and the imposed shear stress applied in the streamwise direction [36,42–44,51,54,55], which can be written as

$$\begin{aligned} & \mu[(\partial_y u + \partial_x v)\{1 - (\partial_x h)^2\} + 2\partial_x h(\partial_y v - \partial_x u) - \partial_z h(\partial_z u + \partial_x w) - \partial_x h \partial_z h(\partial_z v + \partial_y w)] \\ & + \gamma[\partial_x T + \partial_x h \partial_y T] \sqrt{1 + (\partial_x h)^2 + (\partial_z h)^2} = \tau_s \sqrt{1 + (\partial_x h)^2 + (\partial_z h)^2}, \end{aligned} \quad (9)$$

$$\begin{aligned} & \mu[(\partial_y w + \partial_z v)\{1 - (\partial_z h)^2\} + 2\partial_z h(\partial_y v - \partial_z w) - \partial_x h(\partial_z u + \partial_x w) - \partial_x h \partial_z h(\partial_y u + \partial_x v)] \\ & + \gamma[\partial_z T + \partial_z h \partial_y T] \sqrt{1 + (\partial_x h)^2 + (\partial_z h)^2} = 0, \end{aligned} \quad (10)$$

$$\begin{aligned} & P_a - p[1 + (\partial_x h)^2 + (\partial_z h)^2] + 2\mu[\partial_x u(\partial_x h)^2 + \partial_z w(\partial_z h)^2 + \partial_x h \partial_z h(\partial_z u + \partial_x w) - \partial_x h(\partial_y u + \partial_x v) \\ & - \partial_z h(\partial_z v + \partial_y w) + \partial_y v] \\ & = \sigma[\partial_{xx} h\{1 + (\partial_z h)^2\} + \partial_{zz} h\{1 + (\partial_x h)^2\} - 2\partial_x h \partial_z h \partial_{xz} h]\{1 + (\partial_x h)^2 + (\partial_z h)^2\}^{-\frac{1}{2}}, \end{aligned} \quad (11)$$

where  $P_a$  is the ambient pressure surrounding the fluid surface. (iii) The heat transfer between air and the fluid surface,  $y = h(x, z, t)$ , due to convection, is described by Newton's law of cooling [28,36,51]

$$\kappa \frac{(\partial_x T \partial_x h - \partial_y T + \partial_z T \partial_z h)}{\sqrt{1 + (\partial_x h)^2 + (\partial_z h)^2}} = \lambda(T - T_a), \quad (12)$$

where  $\lambda$  is the heat transfer coefficient. (iv) To describe the temporal evolution of the fluid surface,  $y = h(x, z, t)$ , we use the kinematic boundary condition

$$\partial_t h + u \partial_x h + w \partial_z h = v. \quad (13)$$

### A. Dimensionless criterion

The governing equations and the associated boundary conditions are made dimensionless by using the following nondimensional variables:

$$\begin{aligned} u^* &= \frac{u}{U_s}, & v^* &= \frac{v}{U_s}, & w^* &= \frac{w}{U_s}, & p^* &= \frac{pd}{\mu U_s}, \\ x^* &= \frac{x}{d}, & y^* &= \frac{y}{d}, & z^* &= \frac{z}{d}, & h^* &= \frac{h}{d}, \\ t^* &= \frac{t U_s}{d}, & \sigma^* &= \frac{\sigma}{\sigma_a}, & T^* &= \frac{T - T_a}{T_w - T_a}, & \tau &= \frac{\tau_s d}{\mu U_s}, \end{aligned} \quad (14)$$

where  $U_s = \rho g d^2 \sin \theta / (2\mu)$  is the streamwise base velocity at the fluid surface without imposed shear stress. For our convenience, the star symbols are removed from the nondimensional variables in the subsequent mathematical expressions. Next, the nondimensional form of the governing equations and the associated boundary conditions can be expressed as

$$\partial_x u + \partial_y v + \partial_z w = 0, \quad (15)$$

$$\text{Re}(\partial_t u + u \partial_x u + v \partial_y u + w \partial_z u) = -\partial_x p + (\partial_{xx} u + \partial_{yy} u + \partial_{zz} u) + 2, \quad (16)$$

$$\text{Re}(\partial_t v + u \partial_x v + v \partial_y v + w \partial_z v) = -\partial_y p + (\partial_{xx} v + \partial_{yy} v + \partial_{zz} v) - 2 \cot \theta, \quad (17)$$

$$\text{Re}(\partial_t w + u \partial_x w + v \partial_y w + w \partial_z w) = -\partial_z p + (\partial_{xx} w + \partial_{yy} w + \partial_{zz} w), \quad (18)$$

TABLE I. List of different nondimensional numbers and their physical interpretations.

Nondimensional number	Mathematical expression	Physical interpretation
Reynolds number (Re)	$\text{Re} = \frac{\rho U_s d}{\mu}$	$\frac{\text{Inertia}}{\text{Viscous force}}$
Marangoni number (Ma)	$\text{Ma} = \frac{\gamma(T_w - T_a)}{\mu U_s}$	$\frac{\text{Marangoni force}}{\text{Viscous force}}$
Weber number (We)	$\text{We} = \frac{\sigma_a}{\mu U_s}$	$\frac{\text{Force due to surface tension}}{\text{Viscous force}}$
Biot number (Bi)	$\text{Bi} = \frac{\lambda d}{\kappa}$	$\frac{\text{Heat convection at fluid surface}}{\text{Heat conduction within fluid}}$
Prandtl number (Pr)	$\text{Pr} = \frac{\rho c_p \nu}{\kappa}$	$\frac{\text{Momentum diffusion}}{\text{Thermal diffusion}}$
Péclet number (Pe)	$\text{Pe} = \text{RePr} = \frac{\rho c_p U_s d}{\kappa}$	$\frac{\text{Advective heat transfer}}{\text{Heat conduction}}$

$$\text{Pe}(\partial_t T + u\partial_x T + v\partial_y T + w\partial_z T) = (\partial_{xx} T + \partial_{yy} T + \partial_{zz} T), \quad (19)$$

$$u = 0, \quad v = 0, \quad w = 0, \quad T = 1, \quad \text{at } y = 0, \quad (20)$$

$$(\partial_y u + \partial_x v)[1 - (\partial_x h)^2] + 2\partial_x h(\partial_y v - \partial_x u) - \partial_z h(\partial_z u + \partial_x w) - \partial_x h\partial_z h(\partial_z v + \partial_y w) + \text{Ma}[\partial_x T + \partial_x h\partial_y T]\sqrt{1 + (\partial_x h)^2 + (\partial_z h)^2} = \tau\sqrt{1 + (\partial_x h)^2 + (\partial_z h)^2}, \quad \text{at } y = h, \quad (21)$$

$$(\partial_y w + \partial_z v)[1 - (\partial_z h)^2] + 2\partial_z h(\partial_y v - \partial_z w) - \partial_x h(\partial_z u + \partial_x w) - \partial_x h\partial_z h(\partial_y u + \partial_x v) + \text{Ma}[\partial_z T + \partial_z h\partial_y T]\sqrt{1 + (\partial_x h)^2 + (\partial_z h)^2} = 0, \quad \text{at } y = h, \quad (22)$$

$$p_a - p[1 + (\partial_x h)^2 + (\partial_z h)^2] + 2[\partial_x u(\partial_x h)^2 + \partial_z w(\partial_z h)^2 + \partial_x h\partial_z h(\partial_z u + \partial_x w) - \partial_x h(\partial_y u + \partial_x v) - \partial_z h(\partial_z v + \partial_y w) + \partial_y v] = (\text{We} - \text{Ma} T)[\partial_{xx} h\{1 + (\partial_z h)^2\} + \partial_{zz} h\{1 + (\partial_x h)^2\} - 2\partial_x h\partial_z h\partial_{xz} h\{1 + (\partial_x h)^2 + (\partial_z h)^2\}^{-\frac{1}{2}}], \quad \text{at } y = h, \quad (23)$$

$$\frac{(\partial_x T \partial_x h - \partial_y T + \partial_z T \partial_z h)}{\sqrt{1 + (\partial_x h)^2 + (\partial_z h)^2}} = \text{Bi} T, \quad \text{at } y = h, \quad (24)$$

$$\partial_t h + u\partial_x h + w\partial_z h = v, \quad \text{at } y = h, \quad (25)$$

where  $p_a = \frac{p_a d}{\mu U_s}$  is the nondimensional ambient pressure and  $\nu = \mu/\rho$  is the kinematic viscosity. Based on the above dimensionless criterion, we have the following nondimensional numbers: the Reynolds number (Re), Marangoni number (Ma), Weber number (We), Biot number (Bi), and Péclet number (Pe), where  $\text{Pe} = \text{Re Pr}$  and Pr is the Prandtl number. The definition of each nondimensional number and its physical interpretation can be found in Table I. As discussed by Kalliadasis *et al.* [56], the above dimensionless numbers depend on the physical properties of the nonisothermal fluid film, base film thickness, temperature difference between fluid and air phases, and inclination angle. Furthermore, they pointed out that the investigation of each dimensionless number in the thermocapillary instability is a difficult task because this is a large set of nondimensional numbers. For this reason, they introduced a relevant set of dimensionless numbers as adopted in the study of Goussis and Kelly [20]

$$G = \frac{2\text{Re}}{\sin \theta} = \frac{gd^3}{\nu^2}, \quad M = \frac{2\gamma(T_w - T_a)}{\rho} \left( \frac{1}{g \sin \theta \nu^4} \right)^{1/3}, \quad B = \frac{\lambda}{\kappa} \left( \frac{\nu^2}{g \sin \theta} \right)^{1/3},$$

where  $G$  is the Galileo number or the modified Reynolds number,  $M$  is the modified Marangoni number, and  $B$  is the modified Biot number. It should be noted that the modified Marangoni number and the modified Biot number are no longer dependent on the base film thickness  $d$ . As our main purpose is to investigate the effects of imposed shear stress and spanwise wave number on the individual unstable modes, we will use the dimensionless numbers  $\text{Re}$ ,  $\text{Ma}$ ,  $\text{We}$ ,  $\text{Bi}$ , and  $\text{Pr}$  according to our choice of scaling. However, the dimensionless groups  $G$ ,  $M$ ,  $B$ , and the Kapitza number  $\text{Ka} = 2\sigma_a/[\rho(v^4 g \sin \theta)^{1/3}]$  will also be used in the present numerical simulation to reproduce the existing results of the literature. To explore the primary instability, it is essential to compute the solution of the unidirectional parallel fluid flow with a constant fluid layer thickness of  $y = 1$ , the so-called base flow. The analytical solution of the base flow equations can be written as

$$\bar{U}(y) = (2 + \tau)y - y^2, \quad 0 \leq y \leq 1, \quad (26)$$

$$\bar{V}(y) = 0, \quad \bar{W}(y) = 0, \quad 0 \leq y \leq 1, \quad (27)$$

$$\bar{P}(y) = 2 \cot \theta (1 - y) + p_a, \quad 0 \leq y \leq 1, \quad (28)$$

$$\bar{T}(y) = 1 - \left( \frac{\text{Bi}}{1 + \text{Bi}} \right) y, \quad 0 \leq y \leq 1. \quad (29)$$

It should be noted that the streamwise velocity  $\bar{U}(y)$  of the base flow is explicitly dependent on the imposed shear stress  $\tau$ , and it is a quadratic polynomial in  $y$ . However, the temperature  $\bar{T}(y)$  of the base flow is dependent on the Biot number  $\text{Bi}$ , and it is a linear polynomial in  $y$ . However, we can see that the Marangoni number  $\text{Ma}$  does not appear in the basic temperature profile  $\bar{T}(y)$  because the Marangoni number is not present in the boundary condition for Newton's law of cooling (24). Obviously, the basic temperature decreases monotonically from a minimum value at the fluid surface and achieves its maximum value at the inclined plane.

### B. Perturbation equations

To examine the primary instability, a three-dimensional infinitesimal perturbation is superimposed on the base flow. Consequently, we can decompose each flow variable into a basic part and a perturbation part

$$u = \bar{U} + u', \quad v = v', \quad w = w', \quad p = \bar{P} + p', \quad T = \bar{T} + T', \quad h = 1 + h', \quad (30)$$

where  $u'$ ,  $v'$ ,  $w'$ ,  $p'$ ,  $T'$ , and  $h'$  represent the perturbation flow quantities, and  $\bar{U}$ ,  $\bar{P}$ , and  $\bar{T}$  represent the base flow quantities. After inserting the variable's decomposition (30) into the nondimensional governing equations and the associated boundary conditions (15)–(25) and linearizing with respect to the base flow solution, one can obtain the perturbation equations in the following forms:

$$\partial_x u' + \partial_y v' + \partial_z w' = 0, \quad 0 \leq y \leq 1, \quad (31)$$

$$\text{Re}(\partial_t u' + \bar{U} \partial_x u' + v' \partial_y \bar{U}) = -\partial_x p' + (\partial_{xx} u' + \partial_{yy} u' + \partial_{zz} u'), \quad 0 \leq y \leq 1, \quad (32)$$

$$\text{Re}(\partial_t v' + \bar{U} \partial_x v') = -\partial_y p' + (\partial_{xx} v' + \partial_{yy} v' + \partial_{zz} v'), \quad 0 \leq y \leq 1, \quad (33)$$

$$\text{Re}(\partial_t w' + \bar{U} \partial_x w') = -\partial_z p' + (\partial_{xx} w' + \partial_{yy} w' + \partial_{zz} w'), \quad 0 \leq y \leq 1, \quad (34)$$

$$\text{Pe}(\partial_t T' + \bar{U} \partial_x T' + v' \partial_y \bar{T}) = (\partial_{xx} T' + \partial_{yy} T' + \partial_{zz} T'), \quad 0 \leq y \leq 1, \quad (35)$$

$$u' = 0, \quad v' = 0, \quad w' = 0, \quad T' = 0, \quad \text{at } y = 0, \quad (36)$$

$$\partial_y u' + \partial_x v' - 2h' = -\text{Ma} \left[ \partial_x T' - \frac{\text{Bi}}{1 + \text{Bi}} \partial_x h' \right], \quad \text{at } y = 1, \quad (37)$$



$$\partial_y w' + \partial_z v' = -\text{Ma} \left[ \partial_z T' - \frac{\text{Bi}}{1 + \text{Bi}} \partial_z h' \right], \quad \text{at } y = 1, \quad (38)$$

$$-p' + 2 \cot \theta h' + 2 \partial_y v' - 2 \tau \partial_x h' = \left( \text{We} - \frac{\text{Ma}}{1 + \text{Bi}} \right) (\partial_{xx} h' + \partial_{zz} h'), \quad \text{at } y = 1, \quad (39)$$

$$\partial_y T' = \text{Bi} \left( \frac{\text{Bi}}{1 + \text{Bi}} h' - T' \right), \quad \text{at } y = 1, \quad (40)$$

$$\partial_t h' + (1 + \tau) \partial_x h' = v', \quad \text{at } y = 1. \quad (41)$$

### C. Orr-Sommerfeld-type boundary value problem

Now, the solution of the perturbation equations (31)–(41) is assumed in the normal mode form [36,57]

$$\left. \begin{aligned} u'(x, y, z, t) &= \hat{u}(y) \exp[i(k_x x + k_z z - \omega t)], \\ v'(x, y, z, t) &= \hat{v}(y) \exp[i(k_x x + k_z z - \omega t)], \\ w'(x, y, z, t) &= \hat{w}(y) \exp[i(k_x x + k_z z - \omega t)], \\ T'(x, y, z, t) &= \hat{T}(y) \exp[i(k_x x + k_z z - \omega t)], \\ p'(x, y, z, t) &= \hat{p}(y) \exp[i(k_x x + k_z z - \omega t)], \\ h'(x, z, t) &= \hat{h} \exp[i(k_x x + k_z z - \omega t)], \end{aligned} \right\} \quad (42)$$

where  $\hat{u}(y)$ ,  $\hat{v}(y)$ ,  $\hat{w}(y)$ ,  $\hat{T}(y)$ ,  $\hat{p}(y)$ , and  $\hat{h}$  are, respectively, the amplitudes of the perturbation velocity components, perturbation temperature, perturbation pressure, and fluid surface deformation. Here,  $k_x$  and  $k_z$  are the streamwise and spanwise wave numbers,  $\omega = k_x c$  is the angular frequency,  $c$  is the wave speed, and  $k = \sqrt{k_x^2 + k_z^2}$  is the total wave number of the infinitesimal perturbation [58]. Substituting the normal mode solution (42) in the perturbation equations (31)–(41) and eliminating the terms involving pressure, the following coupled system of boundary value problems are obtained for the perturbation normal velocity and perturbation temperature, respectively,

$$(D^2 - k^2)^2 \hat{v} = i \text{Re} \left[ (k_x \bar{U} - \omega)(D^2 - k^2) - k_x \frac{d^2 \bar{U}}{dy^2} \right] \hat{v}, \quad 0 \leq y \leq 1, \quad (43)$$

$$(D^2 - k^2) \hat{T} = \text{Pe} \left[ i(k_x \bar{U} - \omega) \hat{T} + \frac{d \bar{T}}{dy} \hat{v} \right], \quad 0 \leq y \leq 1, \quad (44)$$

$$\hat{v} = 0, \quad \hat{T} = 0, \quad D \hat{v} = 0, \quad \text{at } y = 0, \quad (45)$$

$$(D^2 + k^2) \hat{v} + k^2 \text{Ma} \left[ \hat{T} - \frac{\text{Bi}}{1 + \text{Bi}} \hat{h} \right] + 2i k_x \hat{h} = 0, \quad \text{at } y = 1, \quad (46)$$

$$\begin{aligned} &D^3 \hat{v} - 3k^2 D \hat{v} + i \text{Re}[(\omega - k_x) D \hat{v} - k_x \tau D \hat{v} + k_x \tau \hat{v}] \\ &= k^2 \hat{h} \left[ k^2 \left( \text{We} - \frac{\text{Ma}}{1 + \text{Bi}} \right) + 2 \cot \theta - 2i k_x \tau \right], \quad \text{at } y = 1, \end{aligned} \quad (47)$$

$$D \hat{T} + \text{Bi} \left[ \hat{T} - \frac{\text{Bi}}{1 + \text{Bi}} \hat{h} \right] = 0, \quad \text{at } y = 1, \quad (48)$$

$$\hat{v} + i[\omega - k_x(1 + \tau)] \hat{h} = 0, \quad \text{at } y = 1, \quad (49)$$

where  $D = \frac{d}{dy}$  is the differential operator. Here, the temporal stability analysis will be deciphered and, thereby, the wave number  $k$  will be taken as a real number, while the wave speed  $c$  or, equivalently, the angular frequency  $\omega$  will be taken as a complex number [59].

### III. ANALYTICAL SOLUTION OF THE ORR-SOMMERFELD-TYPE BOUNDARY VALUE PROBLEM

#### A. Long-wave solution

To carry out the primary instability, the long-wave analysis [6] is utilized. As stated by Squire [57,60], the three-dimensional disturbances associated with the H-mode and shear mode are less unstable than those of the two-dimensional ones. Consequently, the long-wave analysis is performed for the two-dimensional infinitesimal disturbances of large wavelengths, i.e.,  $k_x = k(\ll 1)$  and  $k_z = 0$ . The derivation of Squire's theorem for the shear-imposed nonisothermal fluid flow is rendered in Appendix A. Now, we introduce the perturbation stream function  $\psi'(x, y, t)$  by using the following relations:

$$u'(x, y, t) = \partial_y \psi', \quad v'(x, y, t) = -\partial_x \psi', \quad (50)$$

where the perturbation stream function is considered in the normal mode form

$$\psi'(x, y, t) = \hat{\phi}(y) \exp[ik(x - ct)], \quad (51)$$

where  $\hat{\phi}(y)$  is the amplitude of the perturbation stream function. With the help of Eq. (51), one can get  $\hat{v}(y) = -ik\hat{\phi}(y)$ . Next, the expression of  $\hat{v}(y)$  is inserted in the coupled system of boundary value problems (43)–(49). After that, the variables  $\hat{\phi}$ ,  $\hat{T}$ ,  $\hat{\eta}$ , and  $c$  are expanded in infinite series forms in the limit  $k \rightarrow 0$

$$\left. \begin{aligned} \hat{\phi}(y) &= \sum_{n=0}^{\infty} \phi_n k^n, & \hat{T}(y) &= \sum_{n=0}^{\infty} T_n k^n, \\ \hat{\eta} &= \sum_{n=0}^{\infty} \eta_n k^n, & c &= \sum_{n=0}^{\infty} c_n k^n, \end{aligned} \right\} \quad (52)$$

where  $n$  is a nonnegative integer.

#### B. Zeroth-order approximation

After inserting Eq. (52) into the boundary value problems (43)–(49), we collect the leading-order/zeroth-order [ $\mathcal{O}(k^0)$ ] equations

$$D^4 \phi_0(y) = 0, \quad D^2 T_0(y) = 0, \quad 0 \leq y \leq 1, \quad (53)$$

$$\phi_0(y) = 0, \quad T_0(y) = 0, \quad D\phi_0(y) = 0, \quad \text{at } y = 0, \quad (54)$$

$$D^2 \phi_0(y) - 2\eta_0 = 0, \quad D^3 \phi_0(y) = 0, \quad \text{at } y = 1, \quad (55)$$

$$DT_0(y) + \text{Bi } T_0(y) - \frac{\text{Bi}^2}{1 + \text{Bi}} \eta_0 = 0, \quad \text{at } y = 1, \quad (56)$$

$$\phi_0(y) - (c_0 - 1 - \tau)\eta_0 = 0, \quad \text{at } y = 1. \quad (57)$$

The solution of the leading-order/zeroth-order equations (53)–(57) can be expressed as

$$\phi_0(y) = \eta_0 y^2, \quad T_0(y) = \frac{\text{Bi}^2 \eta_0 y}{(1 + \text{Bi})^2}. \quad (58)$$

It should be noted that the leading-order solution  $\phi_0(y)$  is independent of the imposed shear stress  $\tau$ , while the leading-order temperature  $T_0(y)$  depends on the Biot number  $\text{Bi}$ , but it is independent of the Marangoni number  $\text{Ma}$  and the Péclet number  $\text{Pe}$ . Using the leading-order kinematic boundary condition (57), we get the leading-order/zeroth-order phase speed  $c_0$  for the H-mode

$$c_0 = 2 + \tau. \quad (59)$$

Clearly, the leading-order phase speed  $c_0$  for the H-mode is real and increases with the rising values of the imposed shear stress  $\tau$ .

### C. First-order approximation

Collecting the first-order [ $\mathcal{O}(k)$ ] equations, we obtain

$$D^4\phi_1(y) + i\text{Re}[D^2\bar{U}(y)\phi_0(y) + \{c_0 - \bar{U}(y)\}D^2\phi_0(y)] = 0, \quad 0 \leq y \leq 1, \quad (60)$$

$$D^2T_1(y) + i\text{Pe}[D\bar{T}(y)\phi_0(y) + \{c_0 - \bar{U}(y)\}T_0(y)] = 0, \quad 0 \leq y \leq 1, \quad (61)$$

$$\phi_1(y) = 0, \quad T_1(y) = 0, \quad D\phi_1(y) = 0, \quad \text{at } y = 0, \quad (62)$$

$$D^2\phi_1(y) + i\text{Ma}\left[T_0(y) - \frac{\text{Bi}}{1 + \text{Bi}}\eta_0\right] - 2\eta_1 = 0, \quad \text{at } y = 1, \quad (63)$$

$$D^3\phi_1(y) + i\text{Re}[(c_0 - 1)D\phi_0(y) - \tau D\phi_0(y) + \tau\phi_0(y)] - 2i \cot\theta\eta_0 = 0, \quad \text{at } y = 1, \quad (64)$$

$$DT_1(y) + \text{Bi}\left[T_1(y) - \frac{\text{Bi}}{1 + \text{Bi}}\eta_1\right] = 0, \quad \text{at } y = 1, \quad (65)$$

$$\phi_1(y) - (c_0 - 1 - \tau)\eta_1 - c_1\eta_0 = 0, \quad \text{at } y = 1. \quad (66)$$

Here, we assume that the Weber number  $We$  and the Marangoni number  $Ma$  are of order  $\mathcal{O}(1)$ . As a result, these nondimensional numbers are not appearing in the first-order normal stress boundary condition (64). The first-order equations (60)–(66) are solved for the unknown functions  $\phi_1(y)$  and  $T_1(y)$ , which can be found in Appendix B. After substituting the expressions of  $\phi_1(y)$  and  $T_1(y)$  in the first-order kinematic boundary condition (66), one can obtain the expression of  $c_1$  in the following form:

$$c_1 = i(a_0 + a_1\text{Re} + a_2 \cot\theta), \quad (67)$$

where

$$a_0 = \frac{\text{MaBi}}{2(1 + \text{Bi})^2}, \quad a_1 = \frac{4(2 + \tau)}{15}, \quad a_2 = -\frac{2}{3}.$$

Obviously, the expression of  $c_1$  for the H-mode is purely imaginary. Now, the Marangoni number  $Ma$  and the Biot number  $\text{Bi}$  appear in the expression of  $c_1$ . Using the neutral stability condition ( $c_i \approx |kc_i| = 0$ ) in the limit  $k \rightarrow 0$ , one can obtain the critical value of the Reynolds number  $\text{Re}_c$  for the H-mode

$$\text{Re}_c = \frac{5 \cot\theta}{2(2 + \tau)} - \frac{15\text{MaBi}}{8(2 + \tau)(1 + \text{Bi})^2}. \quad (68)$$

It should be noted that a factor  $(2 + \tau)$  is present at the denominator in the expression of  $\text{Re}_c$ . Therefore,  $\text{Re}_c \rightarrow \infty$  as soon as  $\tau \rightarrow -2$ , which implies that the base flow will always be stable to infinitesimal disturbances when  $\tau = -2$ . In fact, this is the physical situation where the leading-order phase speed  $c_0 = (2 + \tau)$  of the infinitesimal disturbance becomes zero and the base flow velocity  $U(y) = [(2 + \tau)y - y^2]$  becomes fully negative in the cross-stream direction. Consequently, the infinitesimal disturbance will not propagate in the streamwise direction. As there is no positive base velocity, the disturbance is not receiving any energy from the base flow to become unstable, which is fully consistent with the result. Furthermore, we see that the analytical expression of the critical Reynolds number  $\text{Re}_c$  for the H-mode coincides with that of Wei [43] for the isothermal viscous fluid flowing down an inclined plane ( $Ma \rightarrow 0$ ,  $\text{Bi} \rightarrow 0$ ) in the absence of insoluble surfactant. Moreover, the critical Reynolds number  $\text{Re}_c$  for the H-mode recovers the result of Trevelyan and Kalliadasis [61] if the effect of imposed shear stress is removed from the fluid surface. From the expression (68), we observe that the critical Reynolds number  $\text{Re}_c$  reduces as the

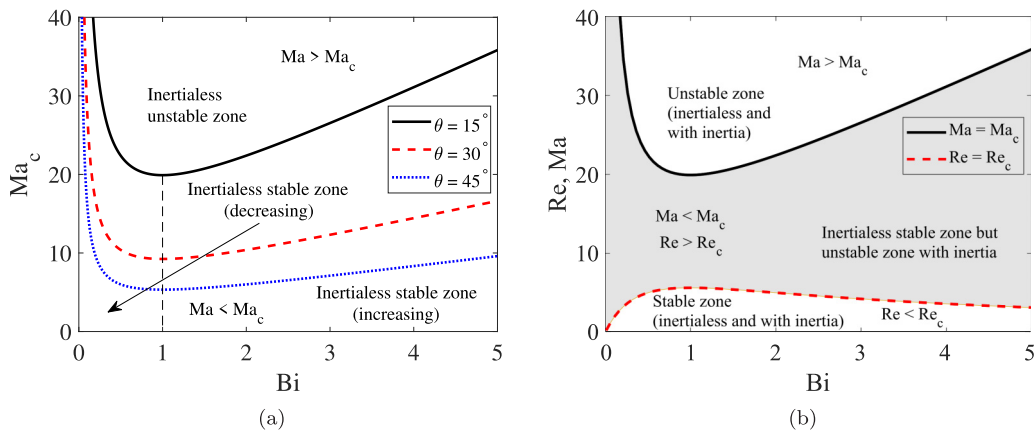


FIG. 2. (a) Variation of the critical Marangoni number  $Ma_c$  with the Biot number  $Bi$  when the inclination angle  $\theta$  alters. Here,  $Ma_c$  is computed from Eq. (69) for the inertialess flow configuration ( $Re = 0$ ). Solid, dashed, and dotted lines stand for  $\theta = 15^\circ$ ,  $\theta = 30^\circ$ , and  $\theta = 45^\circ$ , respectively. (b) Variation of the critical Reynolds number  $Re_c$  with the Biot number  $Bi$  when  $\bar{Ma} = 30$ ,  $\theta = 15^\circ$ , and  $\tau = 0.5$ . Here,  $Re_c$  is computed from Eq. (70). Solid black line stands for  $Ma_c$  and dashed red line stands for  $Re_c$ .

Marangoni number increases, which indicates that increasing the value of the Marangoni number, or equivalently, increasing the value of the surface tension gradient  $\gamma (= -\frac{d\sigma}{dT}|_{T=T_a} > 0)$  has a destabilizing effect on the H-mode. More specifically, the surface instability caused by the H-mode occurs if the Reynolds number is greater than the critical value  $Re_c$ . As reported by Kalliadasis *et al.* [51], the temperature of the fluid is maximum at the crest, while it is minimum at the trough due to the difference in height of the disturbed fluid surface [see Eq. (58)]. As a result, surface tension is minimum at the crest and it is maximum at the trough of the perturbed fluid surface, which creates a flow from the crest to the trough direction on the deformed fluid surface due to the change in surface tension. Now, if the Marangoni number is increased, or equivalently,  $\gamma$  is increased, then the surface tension of the fluid decreases with the rising values of the temperature, preventing flow from occurring in the crest-to-trough direction and producing a destabilizing influence on the H-mode. In other words, the stabilizing effect of surface tension on the H-mode instability becomes weaker as the surface tension reduces with increasing the value of the Marangoni number. Therefore, we can conclude that the nonisothermal flow becomes more unstable than the isothermal flow due to the H-mode in the presence of the Marangoni number. Now, if we set  $Re_c = 0$  in Eq. (68), then we can get the critical value of the Marangoni number  $Ma_c$  for the onset of the inertialess instability

$$Ma_c = \frac{4 \cot \theta (1 + Bi)^2}{3Bi}. \quad (69)$$

Hence, if  $Ma > Ma_c$ , then the inertialess instability occurs in the long-wave regime. In other words, there exists a range of the Marangoni number ( $Ma < Ma_c$ ), where an inertialess nonisothermal fluid flow over an inclined plane can be stabilized to infinitesimal disturbances. The variation of  $Ma_c$  with the Biot number  $Bi$  is demonstrated in Fig. 2(a) when the inclination angle changes. Clearly, we can find two separate zones of the Biot number, divided by a thin vertical dashed line, where two different physical phenomena happen. Initially, the critical value of the Marangoni number decreases up to  $Bi = 1$ , implying a destabilizing effect of the Biot number on the inertialess instability. On the contrary, the critical value of the Marangoni number gradually increases if  $Bi > 1$ , which indicates a stabilizing effect of the Biot number on the inertialess instability. Furthermore, the critical value of the Marangoni number significantly decreases as the inclination angle rises. Therefore, the increasing value of the inclination angle destabilizes the inertialess instability. Finally,  $Ma_c$  becomes zero at  $\theta = \pi/2$ . Hence, an inertialess nonisothermal fluid flow over a vertical plane

will be unstable for any nonzero value of the Marangoni number. Section VII contains a detailed discussion of the inertialess instability. Using Eq. (69), the critical Reynolds number  $Re_c$  for the H-mode can be rewritten as

$$Re_c = \frac{15Bi(Ma_c - Ma)}{8(2 + \tau)(1 + Bi)^2} = \frac{15Bi\bar{Ma}}{8(2 + \tau)(1 + Bi)^2}, \quad (70)$$

where  $\bar{Ma} = (Ma_c - Ma)$ . Obviously, the instability of the H-mode begins for any nonzero value of the Reynolds number when  $Ma = Ma_c$ . However, if  $Ma < Ma_c$  ( $\bar{Ma} > 0$ ), i.e., in the inertialess stable zone, then we can retrieve a range of the Reynolds number, where the nonisothermal flow can be unstable due to inertia. This result is depicted in Fig. 2(b). Furthermore, the critical Reynolds number  $Re_c$  for the H-mode attenuates as the imposed shear stress  $\tau (> 0)$  rises. Therefore, one can expect a destabilizing effect of the imposed shear stress on the primary instability induced by the H-mode.

#### D. Second-order approximation

By collecting the second-order [ $\mathcal{O}(k^2)$ ] equations and solving those equations, we can obtain the expression of  $c_2$  for the H-mode

$$c_2 = \frac{b_0 + b_1Bi + b_2Bi^2 + b_0Bi^3}{120(1 + Bi)^3} + b_3Re Ma Bi + b_4Re \cot \theta + b_5Re^2, \quad (71)$$

where the coefficients  $b_0, b_1, b_2, b_3, b_4,$  and  $b_5$  and the details of the long-wave second-order equations are provided in Appendix C. Clearly,  $c_2$  is real.

#### E. Third-order approximation

Similarly, by collecting and solving the third-order [ $\mathcal{O}(k^3)$ ] equations, one can get the expression of  $c_3$  for the H-mode

$$c_3 = i \left[ \frac{(h_0 - h_1Ma + h_2Ma Pe + h_3Ma Pe^2)}{100800(1 + Bi)^5} - \frac{(h_4 + h_5Ma + h_6Ma^2)Re}{50400(1 + Bi)^4} - \frac{h_7Re^2}{9979200} - \frac{h_8Re^3}{32432400} \right], \quad (72)$$

where the coefficients  $h_i (i = 0, \dots, 8)$  used in the expression of  $c_3$  can be found in Appendix D. Clearly,  $c_3$  is purely imaginary. Combining  $c_0, c_1, c_2,$  and  $c_3$ , the complex wave speed  $c$  for the H-mode can be expressed as

$$c = c_0 + kc_1 + k^2c_2 + k^3c_3 + \mathcal{O}(k^4) = c_r + ic_i. \quad (73)$$

If the imaginary part of the complex wave speed is positive ( $c_i > 0$ ), then the infinitesimal perturbation will grow exponentially with time, and the associated disturbance will be linearly unstable due to the H-mode.

#### F. Padé approximation of the long-wave solutions

Following the works of Lange *et al.* [62] and Pal and Samanta [63], the Padé approximation is applied to improve the result obtained from the fifth-order long-wave solution when the wave number  $k_x \rightarrow 0$ . To this end, the complex wave speed  $c$  for the H-mode is expressed as a ratio of two polynomials in terms of wave number  $k_x = k (k_z = 0)$

$$c = \frac{P_d(k)}{Q_d(k)}, \quad (74)$$

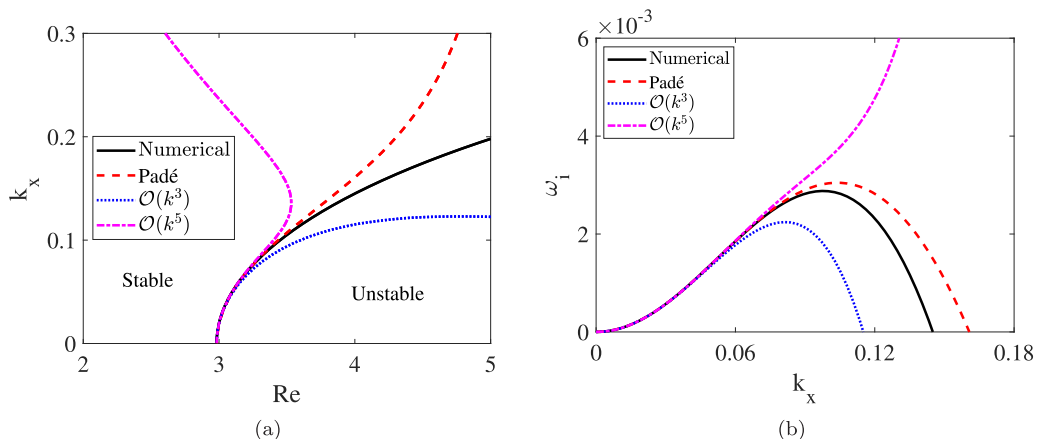


FIG. 3. (a) Comparison of the neutral stability curve for the H-mode with the results computed from the Padé approximation and the numerical simulation in  $(\text{Re}, k_x)$  plane. Here  $k_x = k$  and  $k_z = 0$ . (b) Comparison of the temporal growth rate for the H-mode with the results computed from the Padé approximation and the numerical simulation when  $\text{Re} = 4$ . Solid, dashed, dotted, and dash-dotted lines stand for the results of the numerical simulation, Padé approximation, third-order  $[\mathcal{O}(k^3)]$  long-wave analytical solution, and fifth-order  $[\mathcal{O}(k^5)]$  long-wave analytical solution, respectively. The other parameter values are  $\text{We} = 62.5$ ,  $\text{Pr} = 7$ ,  $\text{Bi} = 1$ ,  $\text{Ma} = 4$ ,  $\theta = 15^\circ$ ,  $\tau = 0.5$ , and  $k_z = 0$ .

where

$$P_d(k) = p_0 + p_1k + p_2k^2 + \dots + p_i k^i, \quad Q_d(k) = 1 + q_1k + q_2k^2 + \dots + q_j k^j \neq 0,$$

where the unknown coefficients  $p_0, p_1, \dots, p_i$  and  $q_1, \dots, q_j$  are determined analytically by using the long-wave solution. Figures 3(a) and 3(b), respectively, display the comparisons of the neutral stability curve and temporal growth rate for the H-mode with the results computed from the Padé approximation and the numerical simulation. The discussion of the numerical technique for solving the boundary value problem (43)–(49) is provided in Sec. IV. Note that the results computed from the Padé approximation capture the results of the numerical simulation in a larger range of wave number than the long-wave analytical solution. In fact, except in the vicinity of the threshold of instability, the long-wave third-order and fifth-order analytical results deviate from the numerical results because the long-wave analytical solution is valid only in the limit  $k \rightarrow 0$  ( $k_x = k, k_z = 0$ ). From the above results, one can conclude that the results obtained from the Padé approximation are more accurate than the results determined from the higher-order long-wave analytical solution.

#### IV. NUMERICAL SOLUTION OF THE ORR-SOMMERFELD-TYPE BOUNDARY VALUE PROBLEMS

Now the boundary value problems (43)–(49) will be solved for the disturbances of arbitrary wave numbers. To do that, we use the Chebyshev spectral collocation method [64]. First, we convert the boundary value problems (43)–(49) into a generalized matrix eigenvalue problem

$$\mathcal{A}\hat{\xi} = \omega\mathcal{B}\hat{\xi}, \quad (75)$$

where  $\omega$  is the eigenvalue with associated eigenvector  $\hat{\xi} = [\hat{v}, \hat{T}, \hat{\eta}]^T$  and the matrices  $\mathcal{A}$  and  $\mathcal{B}$  are of the following forms:

$$\mathcal{A} = \begin{pmatrix} \mathcal{A}_{11} & 0 \\ \mathcal{A}_{21} & \mathcal{A}_{22} \end{pmatrix} \quad \text{and} \quad \mathcal{B} = \begin{pmatrix} \mathcal{B}_{11} & 0 \\ 0 & \mathcal{B}_{22} \end{pmatrix}, \quad (76)$$

where

$$\begin{aligned} \mathcal{A}_{11} &= i\text{Re}k_x[\bar{U}(D^2 - k^2) + 2] - (D^2 - k^2)^2, \\ \mathcal{A}_{21} &= -\frac{\text{Pe Bi}}{1 + \text{Bi}}, \quad \mathcal{A}_{22} = i\text{Pe}k_x\bar{U} - (D^2 - k^2), \\ \mathcal{B}_{11} &= i\text{Re}(D^2 - k^2), \quad \mathcal{B}_{22} = i\text{Pe}, \quad D = \frac{d}{dy}. \end{aligned}$$

Second, the eigenvalue problem (75) is completed by using the boundary conditions (45)–(49). Finally, we expand the amplitude function  $\hat{\xi}(y)$  in a truncated series of the Chebyshev polynomials [57]

$$\hat{\xi}(y) = \sum_{i=0}^N \xi_i P_i(y). \quad (77)$$

Here,  $N$  is the number of Chebyshev polynomials, and  $\xi_i$ 's are the unknown Chebyshev coefficients. In the numerical simulation, we shift the liquid layer domain  $[0, 1]$  to  $[-1, 1]$  by using the transformation  $y = (x + 1)/2$  because the Chebyshev polynomials  $P_i(y)$  are defined over the domain  $[-1, 1]$ . Accordingly, we replace the derivatives  $D \rightarrow 2D$ ,  $D^2 \rightarrow 4D^2$ , ... in the numerical code. After substitution of Eq. (77) into the matrix eigenvalue problem (75), we evaluate the Chebyshev functions at the Gauss-Lobatto collocation points  $x_j = \cos(\pi j/N)$ , which are extrema of the Chebyshev polynomials, where  $j = 0, \dots, N$ .

#### A. Validation of the numerical code

In this subsection, we shall validate our numerical results with the existing results available in the literature. First, we shall compare our numerical result with that of Ding *et al.* [31] when  $\tau = 0$ . Consequently, we choose the flow parameter values of  $\text{Re} = 15$ ,  $\text{We} = 2000$ ,  $\theta = \pi/2$ ,  $\text{Pr} = 0.01$ ,  $B = 1$ ,  $\tau = 0$ , and  $k_z = 0$ . Furthermore, the Marangoni number  $\text{Ma}$  and the Biot number  $\text{Bi}$  are rescaled by the following relations:  $\text{Ma} = M/(2\text{Re})^{2/3}$  and  $\text{Bi} = B(2\text{Re})^{1/3}$ . Figure 4(a) demonstrates the temporal growth rate of the H-mode for three distinct values of  $M$  or, equivalently, for three distinct values of the Marangoni number  $\text{Ma}$ . Obviously, the current numerical code recovers the result of Ding *et al.* [31] in the absence of imposed shear stress when  $M = 0$ . We see that the temporal growth rate  $\omega_j$  for the H-mode becomes stronger as the Marangoni number rises, which implies a destabilizing influence of the Marangoni number on the H-mode. This result is expected because the critical Reynolds number  $\text{Re}_c$  for the H-mode reduces with the increasing value of the Marangoni number in comparison to that of the isothermal flow [see Eq. (68)]. Second, we have reproduced the results of Hu *et al.* [25] when the Soret number and the imposed shear stress are set to zero in the numerical simulation. In Fig. 4(b), the neutral stability curves are plotted in  $(k_x, G)$  plane for distinct values of  $M$  when  $\text{Ka} = 1569.2$ ,  $\theta = 15^\circ$ ,  $\text{Pr} = 10$ ,  $B = 0.03$ ,  $\tau = 0$ , and  $k_z = 0$ . In particular, the numerical results are exhibited for the H-mode and the thermocapillary S-mode. Again an excellent agreement is observed between the current results and the results reported in Hu *et al.* [25] when  $M = 156.92$ . It should be noted that only one neutral stability curve for the H-mode specified by a solid line appears in  $(k_x, G)$  plane when  $M = 0$ , because this is the situation of the isothermal flow configuration. However, two neutral stability curves emerge if  $M$  or, equivalently, the Marangoni number  $\text{Ma}$  keeps a nonzero value. More specifically, the neutral stability curve pertaining to the S-mode appears in the low Galileo number regime, while the neutral stability curve pertaining to the H-mode appears in the moderate Galileo number regime, which are specified by the dashed lines in  $(k_x, G)$  plane when  $M = 156.92$ . Clearly, the critical Galileo number for the onset of H-mode instability and the critical Galileo number for the onset of S-mode stability lie on the  $G$  axis ( $k_x = 0$ ) when  $M = 156.92$ . Actually, the H-mode instability begins due to the infinitesimal

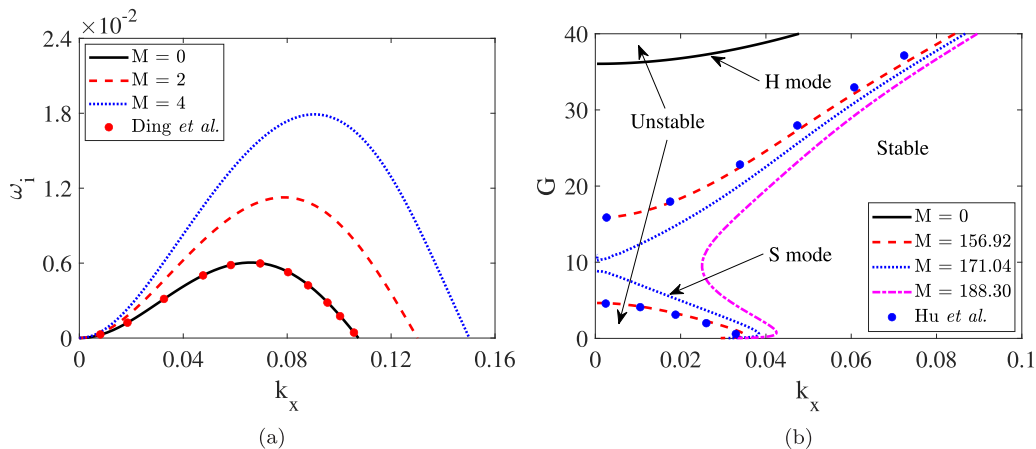


FIG. 4. (a) Variation of the temporal growth rate  $\omega_i$  for the H-mode with streamwise wave number  $k_x$  for different values of  $M$  when  $\text{Re} = 15$ ,  $\text{We} = 2000$ ,  $\theta = \pi/2$ ,  $\text{Pr} = 0.01$ ,  $B = 1$ ,  $\tau = 0$ , and  $k_z = 0$ . Solid, dashed, and dotted lines stand for  $M = 0$ ,  $M = 2$ , and  $M = 4$ , respectively. The solid points are the results of Ding *et al.* [31]. (b) Variation of the neutral stability curves in  $(k_x, G)$  plane for different values of  $M$  when  $\text{Ka} = 1569.2$ ,  $\theta = 15^\circ$ ,  $\text{Pr} = 10$ ,  $B = 0.03$ ,  $\tau = 0$ , and  $k_z = 0$ . Solid, dashed, dotted, and dash-dotted lines stand for  $M = 0$ ,  $M = 156.92$ ,  $M = 171.04$ , and  $M = 188.3$ , respectively. The solid points are the results of Hu *et al.* [25].

perturbation of the fluid surface in the long-wave regime when the Galileo number exceeds the critical value. However, the S-mode instability induced by the Marangoni stress begins in the long-wave regime due to the infinitesimal temperature perturbation at the fluid surface when the Galileo number is very low ( $G \rightarrow 0$ ). Now, if the Galileo number is increased, then inertia becomes stronger and gradually dominates the Marangoni force induced by the variation in surface tension due to the change in temperature. As a result, the S-mode instability becomes weaker and finally becomes stable as the Galileo number rises. Furthermore, we observe that there exists a range of the Galileo number where the S-mode instability is stable to infinitesimal temperature perturbation when  $M = 156.92$ . The above facts indicate that inertia stabilizes the thermocapillary S-mode instability. If the Galileo number is further increased, then the H-mode instability begins when the Galileo number is greater than its critical value. However, there exists a range of the Galileo number where both the H-mode and the S-mode are fully damped to infinitesimal perturbations when  $M = 156.92$ . Instead, if the Marangoni number or, equivalently,  $M$  is increased, then the neutral stability curves for the S-mode and H-mode approach toward each other and finally coalesce with each other and generate a single neutral stability curve at  $M = 188.3$ . In this case, the onset of stability to infinitesimal perturbation moves in the finite streamwise wave number regime when  $M = 188.3$  and  $k_z = 0$ . This physical fact indicates a destabilizing impact of the Marangoni number on the primary instability. To validate the analytical result, the critical Reynolds number for the H-mode is computed numerically and compared with that of the analytical result in Table II when the imposed shear stress  $\tau$  changes. We can clearly see that the numerical results capture the analytical results very well when  $\text{Ka} = 500$ ,  $\theta = 15^\circ$ ,  $\text{Pr} = 7$ ,  $B = 1$ , and  $M = 18$ . Furthermore, the critical Reynolds number for the H-mode decreases with the increasing value of  $\tau$ , but increases with the decreasing value of  $\tau$ . This result indicates that the imposed shear stress destabilizes the H-mode instability if it applies in the coflow direction, but stabilizes the H-mode instability if it applies in the counterflow direction. Actually, the base flow velocity accelerates as the magnitude of the imposed shear stress increases. As a result, the perturbation gets more energy from base flow, that makes stronger the kinetic energy of the perturbation and causes a destabilizing effect on the H-mode instability [65].



TABLE II. Comparison between the analytical and numerical values of the critical Reynolds number  $Re_c$  for the H-mode when the imposed shear stress  $\tau$  changes. The other parameter values are  $Ka = 500$ ,  $\theta = 15^\circ$ ,  $Pr = 7$ ,  $B = 1$ , and  $M = 18$ .

$\tau$	Analytical value ( $Re_c$ )	Numerical value ( $Re_c$ )
-1.0	8.2780	8.2722
-0.5	5.2031	5.2034
0.0	3.6599	3.6562
0.5	2.7256	2.7278
1.0	2.0830	2.0831

### B. Convergence of the spectrum

This subsection deals with the convergence of the spectrum computed from the matrix eigenvalue problem (75) as the flow parameters change. Consequently, we introduce the relative error as defined by Tilton and Cortelezzi [66] and Samanta [67]

$$E_N = \|\mathbf{c}_{N+1} - \mathbf{c}_N\|_2 / \|\mathbf{c}_N\|_2, \quad (78)$$

where  $\|\cdot\|_2$  represents the  $L_2$  norm. Here, we have taken twenty least stable eigenvalues to compute the relative error  $E_N$  when the flow parameters vary. The ensuing results are demonstrated in Fig. 5. In the numerical simulation, we have changed the values of the Marangoni number and the imposed shear stress, while the other parameter values are fixed at  $Re = 5000$ ,  $Ka = 500$ ,  $\theta = 15^\circ$ ,  $Pr = 7$ ,  $B = 1$ ,  $k_x = 1$ , and  $k_z = 0$ . In all cases, we see that the relative error  $E_N$  of the spectrum approximately converges in the range  $[\mathcal{O}(10^{-6}), \mathcal{O}(10^{-5})]$  for  $N \geq 60$ . These results indicate that sixty to one hundred Chebyshev polynomials are sufficient for achieving accurate numerical results from the eigenvalue problem (75). The numerical simulations recognize the existence of three distinct modes, which are called the H-mode, S-mode, and P-mode. More specifically, these modes are emerged for low to moderate values of the Reynolds number, and they are distinguished by their phase speeds, which are fully different from each other. However, when the Reynolds number

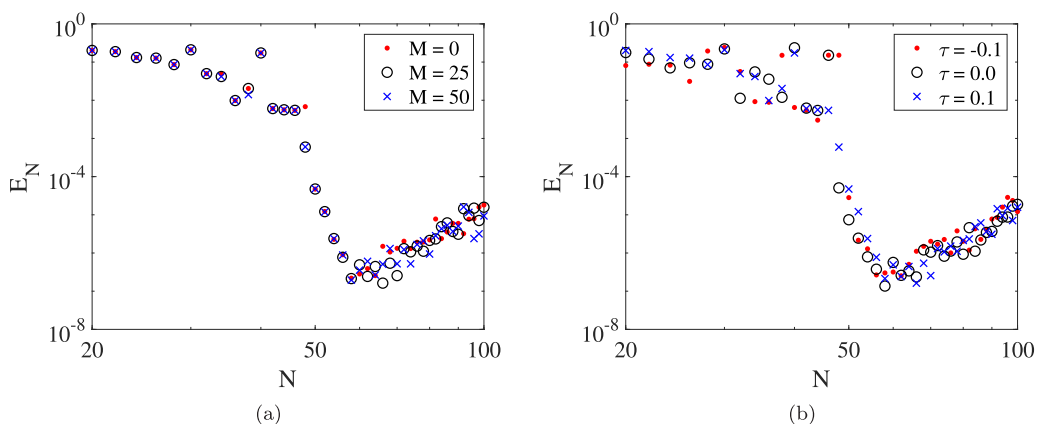


FIG. 5. (a) Variation of the relative error  $E_N$  with the number of Chebyshev polynomials  $N$  for different values of  $M$  when  $Re = 5000$ ,  $Ka = 500$ ,  $\theta = 15^\circ$ ,  $Pr = 7$ ,  $B = 1$ ,  $\tau = 0.1$ ,  $k_x = 1$ , and  $k_z = 0$ . Solid, circle, and cross points stand for  $M = 0$ ,  $M = 25$ , and  $M = 50$ , respectively. (b) Variation of the relative error  $E_N$  with the number of Chebyshev polynomials  $N$  for different values of  $\tau$  when  $Re = 5000$ ,  $Ka = 500$ ,  $\theta = 15^\circ$ ,  $Pr = 7$ ,  $B = 1$ ,  $M = 25$ ,  $k_x = 1$ , and  $k_z = 0$ . Solid, circle, and cross points stand for  $\tau = -0.1$ ,  $\tau = 0$ , and  $\tau = 0.1$ , respectively.

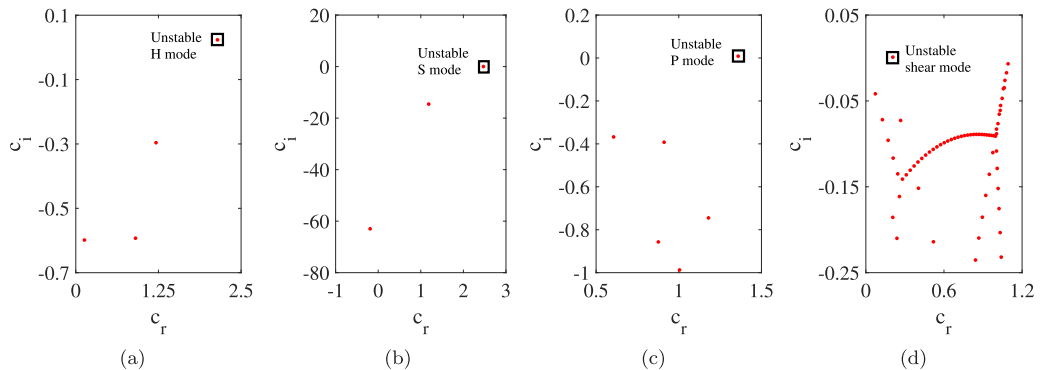


FIG. 6. (a) The eigenvalues in  $(c_r, c_i)$  plane when  $Re = 15$ ,  $\theta = 15^\circ$ ,  $k_x = 0.4$ ,  $M = 25$ ,  $Ka = 500$ , and  $\tau = 0.5$ . (b) The eigenvalues in  $(c_r, c_i)$  plane when  $Re = 0.4$ ,  $\theta = 15^\circ$ ,  $k_x = 0.1$ ,  $M = 30$ ,  $Ka = 500$ , and  $\tau = 0.5$ . (c) The eigenvalues in  $(c_r, c_i)$  plane when  $Re = 10$ ,  $\theta = 15^\circ$ ,  $k_x = 3$ ,  $M = 50$ ,  $Ka = 500$ , and  $\tau = 0.5$ . (d) The eigenvalues in  $(c_r, c_i)$  plane when  $Re = 6000$ ,  $\theta = (1^\circ/60)$ ,  $k_x = 2.2$ ,  $M = 50$ ,  $Ka = 51000$ , and  $\tau = 0.1$ . The other parameter values are  $Pr = 7$ ,  $B = 1$ , and  $k_z = 0$ .

is very large, an additional shear mode [8–10,68,69] is also emerged numerically in the finite streamwise wave number regime. We have depicted these distinct modes in Fig. 6 for the different sets of parameter values. Clearly, the H-mode, S-mode, P-mode, and shear mode have distinct phase speeds.

## V. RESULTS IN LOW TO MODERATE REYNOLDS NUMBER REGIME

### A. Effect of the imposed shear stress

In this subsection, we will explore the sole effect of the imposed shear stress on different unstable modes detected in the numerical simulation. Initially, we analyze the results when the constant shear stress is applied in the coflow direction ( $\tau > 0$ ). To this end, we choose the following parameter values:  $Ka = 500$ ,  $\theta = 15^\circ$ ,  $Pr = 7$ ,  $B = 1$ , and  $k_z = 0$ . Figure 7(a) displays the variations of the neutral stability curves for the H-mode and S-mode when the imposed shear stress varies. We can observe that two neutral stability curves emerge in  $(Re, k_x)$  plane when  $\tau = 0$  and  $M = 25$ . In particular, the neutral stability curve pertaining to the S-mode arises in the low Reynolds number regime, while the neutral stability curve pertaining to the H-mode arises in the moderate Reynolds number regime. As the imposed shear stress increases, the onset of instability for the H-mode moves to the left, and the associated unstable region magnifies. On the contrary, the onset of stability for the S-mode moves to the right, and the associated stable region contracts with the increasing value of the imposed shear stress. These results can also be found in the inset of Fig. 7(a). Due to the above physical phenomena, the onset of instability for the H-mode and the onset of stability for the S-mode merge with each other and, ultimately, generate a single onset of stability as the imposed shear stress rises. Clearly, the unstable zones for the H-mode and S-mode significantly enhance with the increasing values of the imposed shear stress, implying a destabilizing impact on the H-mode and S-mode. Next, we produce the result for the P-mode. Figure 7(b) illustrates the variation of the neutral stability curve for the P-mode when the imposed shear stress changes. In this case, the neutral stability curve arises in the form of a close-island-shape rather than the open-domain-shape emerged for the H-mode when  $\tau = 0$ . It is worth noting that the unstable region for the P-mode appears in the finite streamwise wave number regime instead of the long-wave regime. As long as the imposed shear stress increases, the unstable region for the P-mode gradually shrinks and eventually becomes a point at  $\tau \approx 1.07$ . This fact indicates a stabilizing impact of the imposed shear stress on the P-mode. If we further increase the value of  $\tau$ , then the unstable

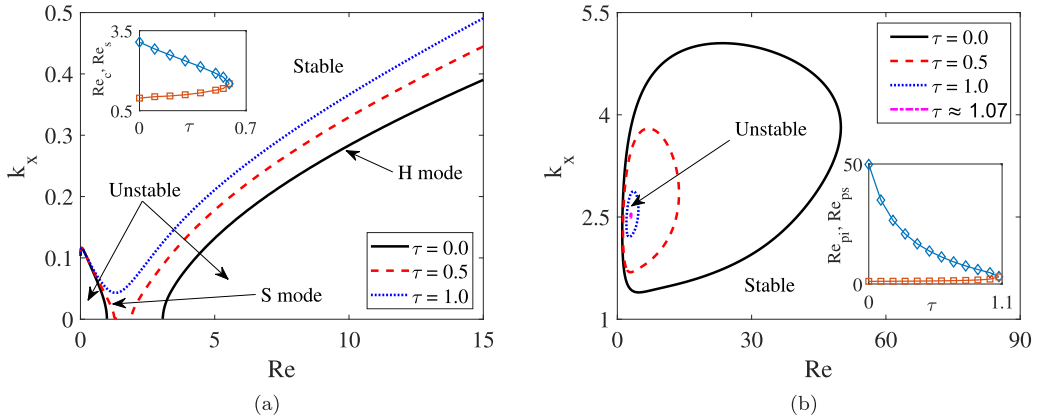


FIG. 7. (a) Variation of the neutral stability curves for the H-mode and the S-mode in  $(Re, k_x)$  plane for different values of the imposed shear stress  $\tau \geq 0$  when  $M = 25$ . Solid, dashed, and dotted lines stand for  $\tau = 0, \tau = 0.5$ , and  $\tau = 1$ , respectively. Variations of the onset of instability  $Re_c$  for the H-mode and the onset of stability  $Re_s$  for the S-mode are shown in the inset of Panel (a). The line with diamond points represents the onset of instability for the H-mode, and the line with square points represents the onset of stability for the S-mode. (b) Variation of the neutral stability curve for the P-mode in  $(Re, k_x)$  plane for different values of the imposed shear stress  $\tau \geq 0$  when  $M = 50$ . Solid, dashed, dotted, and dash-dotted lines stand for  $\tau = 0, \tau = 0.5, \tau = 1$ , and  $\tau \approx 1.07$ , respectively. Variations of the onset of instability  $Re_{pi}$  and the onset of stability  $Re_{ps}$  for the P-mode are shown in the inset of Panel (b). The line with square points represents the onset of instability for the P-mode, and the line with diamond points represents the onset of stability for the P-mode. The other parameter values are  $Ka = 500, \theta = 15^\circ, Pr = 7, B = 1$ , and  $k_z = 0$ .

region completely disappears from the neutral diagram. The variations of the onset of instability and the onset of stability for the P-mode are exhibited in the inset of Fig. 7(b). Now, we will examine the results for the case when the constant shear stress is acting in the counterflow direction ( $\tau < 0$ ). Accordingly, we prefer the following parameter values:  $Ka = 500, \theta = 15^\circ, Pr = 7, B = 1$ , and  $k_z = 0$ . Figure 8(a) illustrates how the neutral stability curves for the H-mode and S-mode vary as the imposed shear stress changes in the counterflow direction. We can see that a single neutral stability curve arises in  $(Re, k_x)$  plane when  $\tau = 0$  and  $M = 37$ . As soon as the magnitude of imposed shear stress is increased in the counterflow direction, two neutral stability curves appear in  $(Re, k_x)$  plane rather than one. The neutral stability curve associated with the S-mode emerges in the low Reynolds number regime, while the neutral stability curve associated with the H-mode emerges in the moderate Reynolds number regime as before. Clearly, the onset of instability for the H-mode moves to the right, and the associated unstable region attenuates with the increasing value of the imposed shear stress in the counterflow direction. On the contrary, the onset of stability for the S-mode moves to the left, and the associated stable region magnifies as the imposed shear stress increases in the counterflow direction. These results are also shown in the inset of Fig. 8(a). Therefore, if the constant shear stress is applied in the counterflow direction, then one can expect a stabilizing influence of the imposed shear stress on the primary instabilities induced by the H-mode and the S-mode. Now, we will show the result for the P-mode. Figure 8(b) demonstrates how the neutral stability curve for the P-mode changes as the imposed shear stress alters in the counterflow direction. As before, we can observe that the unstable zone for the P-mode appears as a point in the finite streamwise wave number regime when  $\tau \approx -0.066$  and  $M = 35$ . If the magnitude of the imposed shear stress is gradually increased in the counterflow direction, then the unstable region for the P-mode expands and forms a close-island-shape. This result indicates that the primary instability induced by the P-mode can be destabilized by applying a constant shear stress in the counterflow direction. The inset of Fig. 8(b) exhibits the variations of the onset of instability and the onset of

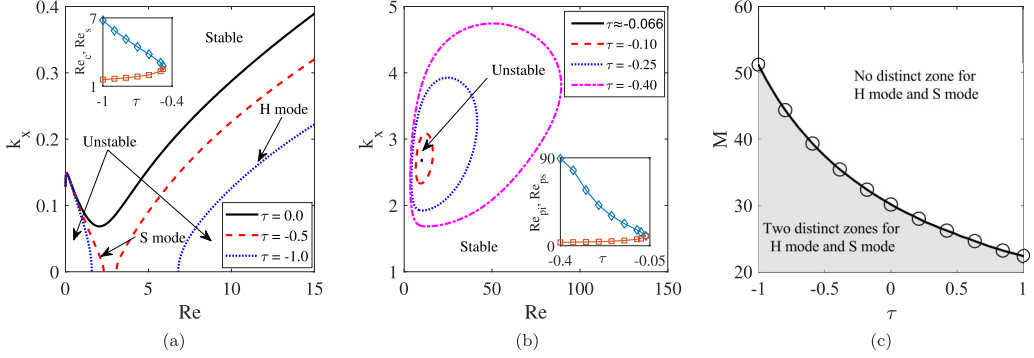


FIG. 8. (a) Variation of the neutral stability curves for the H-mode and the S-mode in  $(\text{Re}, k_x)$  plane for different values of the imposed shear stress  $\tau \leq 0$  when  $M = 37$ . Solid, dashed, and dotted lines stand for  $\tau = 0$ ,  $\tau = -0.5$ , and  $\tau = -1$ , respectively. Variations of the onset of instability  $\text{Re}_c$  for the H-mode and the onset of stability  $\text{Re}_s$  for the S-mode are shown in the inset of Panel (a). The line with diamond points represents the onset of instability for the H-mode, and the line with square points represents the onset of stability for the S-mode. (b) Variation of the neutral stability curve for the P-mode in  $(\text{Re}, k_x)$  plane for different values of the imposed shear stress  $\tau < 0$  when  $M = 35$ . Solid, dashed, dotted, and dash-dotted lines stand for  $\tau \approx -0.066$ ,  $\tau = -0.1$ ,  $\tau = -0.25$ , and  $\tau = -0.40$ , respectively. Variations of the onset of instability  $\text{Re}_{pi}$  and the onset of stability  $\text{Re}_{ps}$  for the P-mode are shown in the inset of Panel (b). The line with square points represents the onset of instability for the P-mode, and the line with diamond points represents the onset of stability for the P-mode. (c) The phase boundary for the existence of distinct unstable zones corresponding to the H-mode and S-mode. The other parameter values are  $\text{Ka} = 500$ ,  $\theta = 15^\circ$ ,  $\text{Pr} = 7$ ,  $B = 1$ , and  $k_z = 0$ .

stability for the P-mode. Furthermore, a close inspection of Figs. 7(a) and 8(a) discloses that there is a special set of values for  $M$  and  $\tau$ , for which the onset of stability for the S-mode and the onset of instability for the H-mode coalesce and, finally, create a single onset for the linear stability to infinitesimal disturbances. In other words, we can retrieve a boundary in  $(\tau, M)$  plane that separates the distinct regimes for the existence of unstable H-mode and S-mode. This phase boundary is calculated numerically and shown in Fig. 8(c). If the parameter values do not belong to the shaded zone, then there are no distinct unstable regimes for the H-mode and S-mode, and a single neutral stability curve appears in  $(\text{Re}, k_x)$  plane. Otherwise, we can obtain separate unstable zones for the H-mode and S-mode in  $(\text{Re}, k_x)$  plane if parameter values belong to the shaded zone.

### B. Effect of the spanwise wave number

This subsection focuses on the sole effect of the spanwise wave number on the individual unstable modes in a low to moderate Reynolds number regime. To produce the results, we choose the following parameter values:  $\text{Ka} = 500$ ,  $\theta = 15^\circ$ ,  $M = 35$ ,  $\text{Pr} = 7$ ,  $B = 1$ , and  $\tau = 0.5$ . Figure 9(a) displays how the neutral stability curves for the H-mode and the S-mode vary as the spanwise wave number  $k_z$  alters. We can see that there is a single neutral stability curve in  $(\text{Re}, k_x)$  plane when the spanwise wave number keeps the value  $k_z = 0$ . If the magnitude of  $k_z$  is increased, then the single neutral stability curve suddenly turns into a pair of separatrices at  $k_z \approx 0.03$ , which is specified by a dashed line. Actually, this is the situation where two neutral stability curves are formed, and both curves are separated by a single point [see Fig. 9(a)]. In particular, one neutral stability curve is associated with the H-mode, while the other neutral stability curve is associated with the S-mode. If the magnitude of  $k_z$  is further increased, then the unstable zones induced by the H-mode and S-mode significantly diminish with the increasing value of  $k_z$ . The interesting result is that the unstable zone created by the H-mode gradually moves upward in the finite streamwise wave number regime as the spanwise wave number rises. By contrast, the unstable zone created by the S-mode gradually moves downward in the long-wave regime and ultimately disappears from

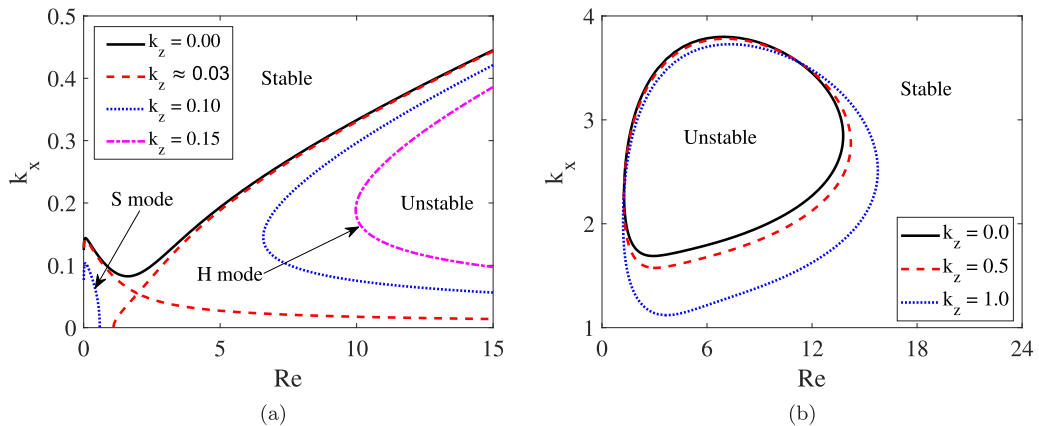


FIG. 9. (a) Variation of the neutral stability curves for the H-mode and S-mode in  $(\text{Re}, k_x)$  plane for different values of the spanwise wave number  $k_z$  when  $M = 35$ . Solid, dashed, dotted, and dash-dotted lines stand for  $k_z = 0$ ,  $k_z \approx 0.03$ ,  $k_z = 0.1$ , and  $k_z = 0.15$ , respectively. (b) Variation of the neutral stability curve for the P-mode in  $(\text{Re}, k_x)$  plane for different values of the spanwise wave number when  $M = 50$ . Solid, dashed, and dotted lines stand for  $k_z = 0$ ,  $k_z = 0.5$ , and  $k_z = 1$ , respectively. The other parameter values are  $\text{Ka} = 500$ ,  $\theta = 15^\circ$ ,  $\text{Pr} = 7$ ,  $B = 1$ , and  $\tau = 0.5$ .

the neutral diagram as the spanwise wave number rises [see Fig. 9(a)]. The above results imply that the H-mode and S-mode instabilities can be suppressed by including the spanwise wave number to the infinitesimal disturbances. It should be noted that the result associated with the H-mode is consistent with the statement of Squire's theorem. Next, we have produced the result for the thermocapillary P-mode. Accordingly, we take the following parameter values:  $\text{Ka} = 500$ ,  $\theta = 15^\circ$ ,  $M = 50$ ,  $\text{Pr} = 7$ ,  $B = 1$ , and  $\tau = 0.5$ . Figure 9(b) reveals how the neutral stability curve for the P-mode varies as the spanwise wave number  $k_z$  changes. Obviously, the neutral stability curve arises in the finite streamwise wave number regime rather than the long-wave regime. It is worth noting that the unstable region generated by the P-mode grows in size with the increasing value of the spanwise wave number. This fact indicates that the spanwise wave number has a destabilizing influence on the P-mode instability. Therefore, the statement of Squire's theorem cannot be applied to the P-mode instability.

## VI. RESULTS IN HIGH REYNOLDS NUMBER REGIME

Now, we will investigate the shear mode when the imposed shear stress varies. In general, the shear mode can be identified numerically when the Reynolds number is very large, but the inclination angle is sufficiently small [8–10]. First, we will produce the results when the constant shear stress acts in the coflow direction ( $\tau > 0$ ). Accordingly, we take the following parameter values:  $\text{Ka} = 51000$ ,  $\theta = (1^\circ/60)$ ,  $\text{Pr} = 7$ ,  $B = 1$ ,  $M = 15$ , and  $k_z = 0$ . Figure 10(a) demonstrates the variation of the neutral stability curve for the shear mode as the imposed shear stress changes. Obviously, the neutral stability curve forms a tongue-like-shape in  $(\text{Re}, k_x)$  plane. We can see that the onset of instability for the shear mode shifts to the left side with the increasing value of the imposed shear stress. This result can also be understood from the inset of Fig. 10(a), where the variation of the critical Reynolds number for the shear mode is displayed with the imposed shear stress. Therefore, one can begin shear mode instability at a lower Reynolds number than the case when the imposed shear stress is absent. By contrast, if the constant shear stress is applied in the counterflow direction ( $\tau < 0$ ), then the onset of instability for the shear mode shifts to the right side [see Fig. 10(b)]. Therefore, the shear mode instability can be delayed by applying a constant shear stress in the counterflow direction. Since, both the H-mode and the shear mode emerge in the

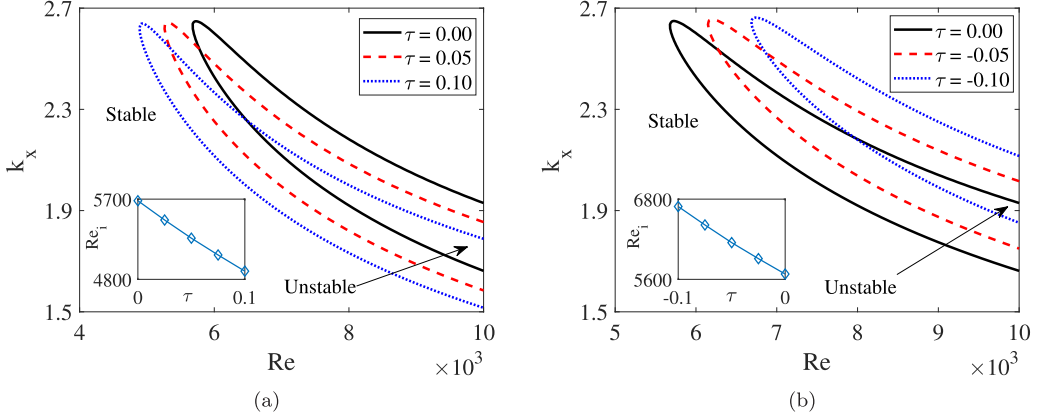


FIG. 10. (a) Variation of the neutral stability curve for the shear mode in  $(Re, k_x)$  plane for different values of the imposed shear stress  $\tau (\geq 0)$ . Solid, dashed, and dotted lines stand for  $\tau = 0$ ,  $\tau = 0.05$ , and  $\tau = 0.1$ , respectively. (b) Variation of the neutral stability curve for the shear mode in  $(Re, k_x)$  plane for different values of the imposed shear stress  $\tau (\leq 0)$ . Solid, dashed, and dotted lines stand for  $\tau = 0$ ,  $\tau = -0.05$ , and  $\tau = -0.1$ , respectively. Variation of the critical Reynolds number  $Re_c$  for the onset of instability corresponding to the shear mode is shown in the inset of Panels (a) and Panels (b), respectively. The other parameter values are  $Ka = 51000$ ,  $\theta = (1^\circ/60)$ ,  $Pr = 7$ ,  $B = 1$ ,  $M = 15$ , and  $k_z = 0$ .

high Reynolds number regime, they can compete with each other to trigger the primary instability at a sufficiently small value of the inclination angle [8,69]. To examine this physical phenomenon, we take the following parameter values:  $Ka = 76000$ ,  $\theta = (1^\circ/60)$ ,  $Pr = 7$ ,  $B = 1$ ,  $M = 10$ , and  $k_z = 0$ . Figure 11(a) depicts two neutral stability curves for the H-mode and the shear mode in  $(Re, k_x)$  plane when  $\tau = 1$ . In this case, we see that the threshold of instability for the shear mode appears at a lower Reynolds number than that of the H-mode [see the dashed line in the inset of Fig. 11(b)]. Hence, the shear mode dominates the primary instability for the given set of parameter values. If the magnitude of the imposed shear stress is gradually decreased, then an interesting

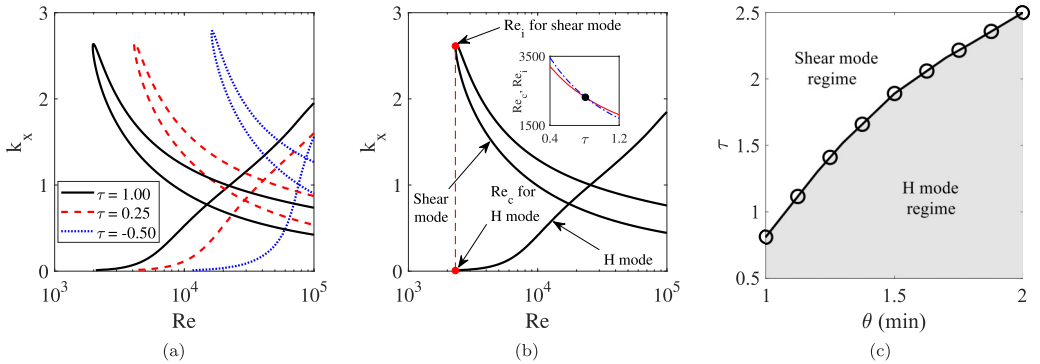


FIG. 11. (a) Variation of the neutral stability curves for the H-mode and the shear mode in  $(Re, k_x)$  plane for different values of the imposed shear stress  $\tau$  when  $\theta = (1^\circ/60)$ . Solid, dashed, and dotted lines stand for  $\tau = 1$ ,  $\tau = 0.25$ , and  $\tau = -0.5$ , respectively. (b) Competition between the H-mode and the shear mode in  $(Re, k_x)$  plane when  $\tau = 0.81$  and  $\theta = (1^\circ/60)$ . Solid and dashed lines in inset figure stand for the variation of the critical Reynolds number for the H-mode and the shear mode, respectively. (c) The phase boundary for the distinct unstable zones corresponding to the H-mode and the shear mode. The other parameter values are  $Ka = 76000$ ,  $Pr = 7$ ,  $B = 1$ ,  $M = 10$ , and  $k_z = 0$ .

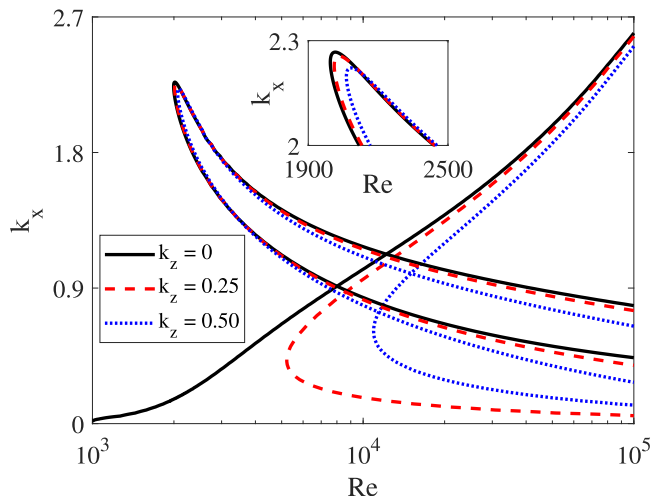


FIG. 12. Variation of the neutral stability curves for the H-mode and the shear mode in  $(\text{Re}, k_x)$  plane for different values of the spanwise wave number  $k_z$ . Solid, dashed, and dotted lines stand for  $k_z = 0$ ,  $k_z = 0.25$ , and  $k_z = 0.50$ , respectively. The other parameter values are  $\text{Ka} = 71096$ ,  $\theta = (3^\circ/60)$ ,  $\text{Pr} = 7$ ,  $B = 1$ ,  $M = 10$ , and  $\tau = 0.5$ .

scenario is perceived. At  $\tau = 0.81$ , the threshold of instabilities for the H-mode and the shear mode appear at the same Reynolds number [see Fig. 11(b)]. In this case, both the H-mode and the shear mode trigger the primary instability. As the threshold of instability for the shear mode attenuates at a faster rate than that for the H-mode with the decreasing value of the imposed shear stress, the threshold of instability for the shear mode is always greater than that of the H-mode as soon as it overtakes the threshold of instability for the H-mode [see the solid line in the inset of Fig. 11(b)]. As a result, the shear mode will have no further chance to drive the primary instability. Consequently, the H-mode dominates the primary instability with the decreasing value of the imposed shear stress. From Fig. 11(b), one can further conclude that there is a special value of  $\tau$  for a given parameter values, for which the critical Reynolds numbers for the H-mode and the shear mode will be the same. In other words, we can find a boundary in  $(\theta, \tau)$  plane that separates the distinct regimes for the H-mode instability and the shear mode instability. This phase boundary is demonstrated in Fig. 11(c). If the parameter values lie in the shaded zone, then the H-mode dominates the primary instability. However, the shear mode dominates the primary instability, if the parameter values do not lie in the shaded zone. To examine the effect of the spanwise wave number on the shear mode, we will produce a similar result, but the spanwise wave number will be varied instead of the imposed shear stress. The result is displayed in Fig. 12. It should be noted that the H-mode dominates the primary instability when  $k_z = 0$ , because the threshold of instability of the H-mode is lower than that of the shear mode. As soon as the magnitude of the spanwise wave number increases, the shear mode triggers the primary instability because the threshold of instability of the shear mode is lower than that of the H-mode. Therefore, the primary instability can be originated by the shear mode by incorporating the spanwise wave number into the infinitesimal disturbance. Furthermore, we notice that the spanwise wave number stabilizes the shear mode instability, as was observed for the H-mode instability. This result is consistent with the statement of Squire's theorem.

## VII. INERTIALESS STABILITY ANALYSIS

To investigate the linear stability analysis for the two-dimensional nonisothermal fluid flow in the inertialess limit, we set  $\text{Re} = 0$ ,  $k_x = k$ , and  $k_z = 0$  [6,28]. As a result, the Orr-Sommerfeld-type

boundary value problems (43)–(49) are simplified into the following forms:

$$(D^2 - k^2)^2 \hat{v} = 0, \quad 0 \leq y \leq 1, \quad (79)$$

$$(D^2 - k^2) \hat{T} = 0, \quad 0 \leq y \leq 1, \quad (80)$$

$$\hat{v} = 0, \quad \hat{T} = 0, \quad D\hat{v} = 0, \quad \text{at } y = 0, \quad (81)$$

$$(D^2 + k^2) \hat{v} + k^2 \text{Ma} \left[ \hat{T} - \frac{\text{Bi}}{1 + \text{Bi}} \hat{\eta} \right] + 2ik\hat{\eta} = 0, \quad \text{at } y = 1, \quad (82)$$

$$D^3 \hat{v} - 3k^2 D\hat{v} = k^2 \hat{\eta} \left[ k^2 \left( \text{We} - \frac{\text{Ma}}{1 + \text{Bi}} \right) + 2 \cot \theta - 2ik\tau \right], \quad \text{at } y = 1, \quad (83)$$

$$D\hat{T} + \text{Bi} \left[ \hat{T} - \frac{\text{Bi}}{1 + \text{Bi}} \hat{\eta} \right] = 0, \quad \text{at } y = 1, \quad (84)$$

$$\hat{v} + i[\omega - k(1 + \tau)] \hat{\eta} = 0, \quad \text{at } y = 1. \quad (85)$$

The general solutions of Eqs. (79) and (80) can be written as

$$\hat{v}(y) = r_1 e^{ky} + r_2 e^{-ky} + r_3 y e^{ky} + r_4 y e^{-ky}, \quad (86)$$

$$\hat{T}(y) = r_5 e^{ky} + r_6 e^{-ky}, \quad (87)$$

where  $r_1, r_2, r_3, r_4, r_5,$  and  $r_6$  are integration constants to be determined from the boundary conditions. Inserting the solutions (86) and (87) in the associated boundary conditions (81)–(85), one can get a homogeneous system of algebraic equations for the unknown variables  $r_1, r_2, r_3, r_4, r_5, r_6,$  and  $\hat{\eta}$ . Next, this system of equations is recast into a matrix equation form [69]

$$\mathcal{M}\mathcal{X} = 0, \quad (88)$$

where

$$\mathcal{M} = \begin{pmatrix} 1 & 1 & 0 & 0 & 0 & 0 & 0 & 0 \\ k & -k & 1 & 1 & 0 & 0 & 0 & 0 \\ 0 & 0 & 0 & 0 & 1 & 1 & 0 & 0 \\ 2k^2 e^k & 2k^2 e^{-k} & 2k(k+1)e^k & 2k(k-1)e^{-k} & k^2 \text{Ma} e^k & k^2 \text{Ma} e^{-k} & \{2ik - \frac{k^2 \text{Ma} \text{Bi}}{(1+\text{Bi})}\} & \\ -2k^3 e^k & 2k^3 e^{-k} & -2k^3 e^k & 2k^3 e^{-k} & 0 & 0 & -k^2 \{2 \cot \theta - 2ik\tau + k^2 (\text{We} - \frac{\text{Ma}}{1+\text{Bi}})\} & \\ 0 & 0 & 0 & 0 & (\text{Bi} + k)e^k & (\text{Bi} - k)e^{-k} & -\frac{\text{Bi}^2}{(1+\text{Bi})} & \\ e^k & e^{-k} & e^k & e^{-k} & 0 & 0 & ik\{c - (1 + \tau)\} & \end{pmatrix}$$

and

$$\mathcal{X} = \begin{pmatrix} r_1 \\ r_2 \\ r_3 \\ r_4 \\ r_5 \\ r_6 \\ \hat{\eta} \end{pmatrix}.$$

Therefore, the determinant of the matrix  $\mathcal{M}$  must be zero for a nontrivial solution of  $\mathcal{X}$ . Hence, we can write

$$\det(\mathcal{M}) = 0, \quad (89)$$

which leads to a dispersion relation in the following form:

$$\text{Disp}(c, k, \text{Ma}, \text{We}, \text{Bi}, \tau, \theta) = 0. \quad (90)$$



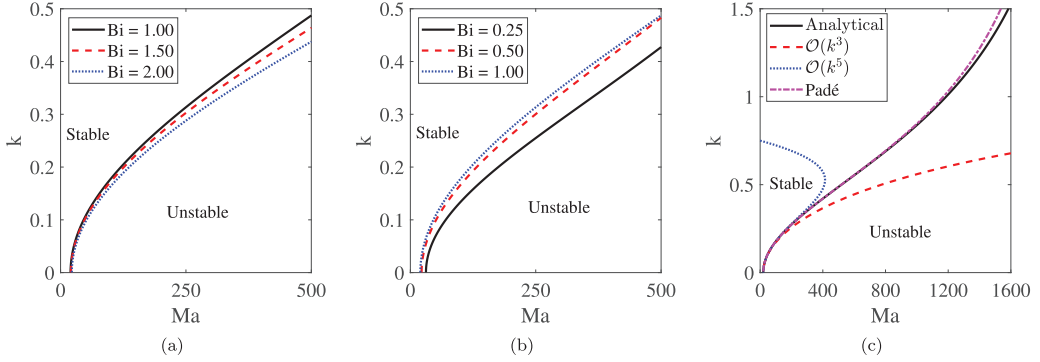


FIG. 13. (a) Variation of the neutral stability curve for the inertialess instability in  $(Ma, k)$  plane for different values of the Biot number ( $Bi \geq 1$ ). Solid, dashed, and dotted lines stand for  $Bi = 1$ ,  $Bi = 1.5$ , and  $Bi = 2$ , respectively. (b) Variation of the neutral stability curve for the inertialess instability in  $(Ma, k)$  plane for different values of the Biot number ( $Bi \leq 1$ ). Solid, dashed, and dotted lines stand for  $Bi = 0.25$ ,  $Bi = 0.5$ , and  $Bi = 1$ , respectively. (c) Comparison of the neutral stability curve for the inertialess instability with the results computed from the Padé approximation and the long-wave solutions in  $(Ma, k)$  plane when  $Bi = 1$ . Solid, dashed, dotted, and dash-dotted lines stand for the results of the dispersion relation (90), third-order [ $\mathcal{O}(k^3)$ ] long-wave analytical solution, fifth-order [ $\mathcal{O}(k^5)$ ] long-wave analytical solution, and the Padé approximation, respectively. The other parameter values are  $We = 1000$ ,  $\theta = 15^\circ$ , and  $k_z = 0$ .

Using the long-wave analysis in the limit  $k \rightarrow 0$ , the complex wave speed  $c$  for the infinitesimal disturbance is determined in the following form:

$$\begin{aligned}
 c = & (2 + \tau) + \frac{i}{6} \left[ \frac{3Ma Bi}{(1 + Bi)^2} - 4 \cot \theta \right] k - \frac{2}{3} (3 + \tau) k^2 \\
 & - \frac{i}{30} \left[ \frac{5Ma \{Bi(2 + 3Bi) - 2\}}{(1 + Bi)^3} + 10We - 36 \cot \theta \right] k^3 \\
 & + \left( \frac{11}{3} + \frac{6\tau}{5} \right) k^4 + \frac{i}{630} \left[ \frac{7Ma \{Bi(3 + 4Bi(33 + 20Bi)) - 54\}}{(1 + Bi)^4} + 378We - 1380 \cot \theta \right] k^5 \\
 & + \mathcal{O}(k^6).
 \end{aligned} \tag{91}$$

Finally, the neutral stability condition ( $c_i \approx |kc_1| = 0$ ) in the limit  $k \rightarrow 0$  provides the critical value of the Marangoni number  $Ma_c$  for the inertialess instability

$$Ma_c = \frac{4 \cot \theta (1 + Bi)^2}{3Bi}. \tag{92}$$

Clearly, Eq. (92) coincides with that given in Eq. (69) for the inertialess instability. Next, we solve the dispersion relation (90) in the arbitrary wave number regime for the complex wave speed  $c$  when the flow parameters are constant. Figures 13(a) and 13(b) depict the neutral stability curve for the inertialess instability in  $(Ma, k)$  plane when the Biot number varies. Obviously, there are two different regimes of the Biot number as demonstrated before. More specifically, the unstable zone for the inertialess instability becomes smaller as the Biot number rises ( $Bi \geq 1$ ), which specifies a stabilizing influence of the Biot number, or equivalently, the heat transfer coefficient on the inertialess instability. By contrast, the unstable zone for the inertialess instability becomes larger as the Biot number rises ( $Bi \leq 1$ ), which specifies a destabilizing influence of the Biot number, or equivalently, the heat transfer coefficient on the inertialess instability. This physical phenomenon was discussed before in Sec. III based on the long-wave stability analysis. However, Fig. 13(c) depicts the comparison of the neutral stability curve for the inertialess instability computed from

the dispersion relation, long-wave analysis, and the Padé approximation, respectively. It should be noted that the result obtained from the Padé approximation is more accurate in comparison with the long-wave third-order and long-wave fifth-order solutions because the result of the Padé approximation arrests the result of the dispersion relation in a larger range of wave number than the long-wave third-order and long-wave fifth-order solutions.

### VIII. INVISCID STABILITY ANALYSIS

This section deals with inviscid stability analysis for the two-dimensional nonisothermal fluid flow in the presence of an imposed shear stress. Therefore, we set the Reynolds number  $Re$  very large [68,70]. In the limit  $Re \rightarrow \infty$ , the Orr-Sommerfeld-type boundary value problems (43)–(49) are reduced to the following Rayleigh-type boundary value problems:

$$[(\bar{U} - c)(D^2 - k^2) - D^2\bar{U}]\hat{\phi} = 0, \quad y \in [0, 1], \quad (93)$$

$$(\bar{U} - c)\hat{T} - D\bar{T}\hat{\phi} = 0, \quad y \in [0, 1], \quad (94)$$

$$\hat{\phi} = 0, \quad \hat{T} = 0, \quad \text{at } y = 0, \quad (95)$$

$$(c - \bar{U})D\hat{\phi} + D\bar{U}\hat{\phi} - \frac{1}{(c - \bar{U})} \left[ k^2 \left( \hat{W}e - \frac{\hat{M}a}{1 + Bi} \right) + 2 \cot \hat{\theta} \right] \hat{\phi} = 0, \quad \text{at } y = 1, \quad (96)$$

where  $\hat{v}(y) = -ik\hat{\phi}$  and  $\omega = kc$ . The new parameters  $\hat{W}e = We/Re$ ,  $\hat{M}a = Ma/Re$ , and  $\cot \hat{\theta} = \cot \theta/Re$  are introduced in Eq. (96) to assess their effects on the unstable growth rate. It should be useful to report here that we assume the new parameters  $\hat{W}e$ ,  $\hat{M}a$ , and  $\cot \hat{\theta}$  are of order  $\mathcal{O}(1)$ . Here,  $c = c_r + ic_i$  is the complex wave speed of the infinitesimal disturbance. Now, to solve the second-order boundary value problems (93)–(96), we first apply the transformation  $\hat{\phi}(y) = (U - c)\Phi(y)$ , which recasts the above Rayleigh-type boundary value problems (93)–(96) into the following forms:

$$D[(\bar{U} - c)^2 D\Phi] - (\bar{U} - c)^2 k^2 \Phi = 0, \quad (97)$$

$$(\bar{U} - c)[\hat{T} - D\bar{T}\Phi] = 0, \quad (98)$$

$$\Phi(0) = 0, \quad \hat{T}(0) = 0, \quad (99)$$

$$(\bar{U} - c)^2 D\Phi(1) - \left[ k^2 \left( \hat{W}e - \frac{\hat{M}a}{1 + Bi} \right) + 2 \cot \hat{\theta} \right] \hat{\phi}(1) = 0. \quad (100)$$

Next, Eq. (97) is multiplied by the complex conjugate function  $\Phi^*$  and integrated with respect to  $y$  over the fluid layer depth  $[0, 1]$ . Finally, the boundary conditions (99) and (100) are used. The above mathematical procedures yield the following equation:

$$\int_0^1 (\bar{U} - c)^2 Q(y) dy = \left[ k^2 \left( \hat{W}e - \frac{\hat{M}a}{1 + Bi} \right) + 2 \cot \hat{\theta} \right] |\Phi(1)|^2, \quad (101)$$

where  $Q(y) = (|D\Phi(y)|^2 + k^2|\Phi(y)|^2) \geq 0$ . Comparing the real and imaginary parts of Eq. (101), one can obtain

$$\int_0^1 [(\bar{U} - c_r)^2 - c_i^2] Q(y) dy - \left[ k^2 \left( \hat{W}e - \frac{\hat{M}a}{1 + Bi} \right) + 2 \cot \hat{\theta} \right] |\Phi(1)|^2 = 0, \quad (102)$$

$$c_i \int_0^1 (\bar{U} - c_r) Q(y) dy = 0. \quad (103)$$

As we want to decipher the instability ( $c_i > 0$ ) for the inviscid nonisothermal fluid flow, the integral (103) will not be vanished for  $c_r > (1 + \tau)$  unless  $Q(y) = 0$ , which in fact indicates a trivial solution. However, we are interested in finding a nontrivial solution. Therefore, for a nontrivial unstable solution, we must have

$$c_r = (1 + \tau/2)^2 - \left[ \frac{\int_0^1 (1 + \tau/2 - y)^2 Q(y) dy}{\int_0^1 Q(y) dy} \right]. \quad (104)$$

After substitution of the expression of  $c_r$  in Eq. (102), one can get the expression of  $c_i$  as follows:

$$c_i^2 = \frac{\int_0^1 (1 + \tau/2 - y)^4 Q(y) dy}{\int_0^1 Q(y) dy} - \left[ \frac{\int_0^1 (1 + \tau/2 - y)^2 Q(y) dy}{\int_0^1 Q(y) dy} \right]^2 - \frac{[k^2(\hat{We} - \frac{\hat{Ma}}{1+\text{Bi}}) + 2 \cot \theta] |\Phi(1)|^2}{\int_0^1 Q(y) dy}. \quad (105)$$

Expression (105) shows that  $c_i^2$ , or equivalently, the growth rate of the inviscid nonisothermal fluid flow accelerates with the increasing value of  $\hat{Ma}$ , but decelerates with the increasing values of  $\hat{We}$  and  $\cot \theta$ . Therefore, one can report that  $\hat{Ma}$  has a destabilizing impact but  $\hat{We}$  and  $\cot \theta$  have a stabilizing impact on the inviscid instability. Furthermore, using Eqs. (102) and (103), we can write

$$\int_0^1 \bar{U}^2 Q(y) dy = \Gamma + (c_r^2 + c_i^2) \int_0^1 Q(y) dy, \quad (106)$$

$$\int_0^1 \bar{U} Q(y) dy = c_r \int_0^1 Q(y) dy, \quad (107)$$

where  $\Gamma = [k^2(\hat{We} - \frac{\hat{Ma}}{1+\text{Bi}}) + 2 \cot \theta] |\Phi(1)|^2$ . Suppose,  $U_{\min}$  and  $U_{\max}$  are the minimum and maximum values of the base velocity  $\bar{U}$ . Then

$$\begin{aligned} 0 &\geq \int_0^1 (U - U_{\min})(U - U_{\max})Q(y) dy \\ &= \Gamma + [c_r^2 + c_i^2 - (U_{\min} + U_{\max})c_r + U_{\min}U_{\max}] \int_0^1 Q(y) dy, \end{aligned} \quad (108)$$

which implies that

$$\left[ c_r - \frac{U_{\max} + U_{\min}}{2} \right]^2 + c_i^2 \leq \left[ \frac{U_{\max} - U_{\min}}{2} \right]^2 - \frac{\Gamma}{\int_0^1 Q dy}. \quad (109)$$

For a nontrivial solution, we have  $\int_0^1 Q dy > 0$ . Now, if we prefer the parameter values such that  $\Gamma > 0$ , or equivalently,  $\hat{We} > \frac{\hat{Ma}}{1+\text{Bi}}$ , then Eq. (109) simplifies into the following form:

$$\left[ c_r - \frac{U_{\max} + U_{\min}}{2} \right]^2 + c_i^2 \leq \left[ \frac{U_{\max} - U_{\min}}{2} \right]^2, \quad (110)$$

which is the mathematical expression for Howard's semicircle theorem. Clearly, for a given set of parameter values with  $\Gamma > 0$ , the eigenvalues of the Rayleigh-type boundary value problems lie within a semicircular disk of radius  $\frac{U_{\max} - U_{\min}}{2}$ , whose center is located at  $c_r = \frac{U_{\max} + U_{\min}}{2}$  and  $c_i = 0$ .

### IX. SUMMARY AND CONCLUSIONS

A linear stability analysis is performed for a gravity-driven three-dimensional shear-imposed thin viscous incompressible film flowing down an inclined plane, where the bounding plane is uniformly heated. As a result, the temperature is constant on the plane. However, the heat transfer due to convection at the fluid surface follows Newton's law of cooling. Depending on the application of the constant shear stress on the fluid surface, the coflow ( $\tau > 0$ ) and the counterflow ( $\tau < 0$ ) problems are thoroughly explored. A coupled system of boundary value problems is developed in terms of the amplitudes of perturbation normal velocity and perturbation temperature to carry out the linear stability analysis, which is solved analytically by using the long-wave series expansion, and is also solved numerically by using the Chebyshev spectral collocation method in the arbitrary wave number regime. The analytical solution shows that the H-mode exists in the long-wave regime, and the critical Reynolds number for the onset of H-mode instability attenuates with the increasing values of the Marangoni number and the shear stress imposed in the coflow direction. This fact implies a destabilizing influence of the Marangoni number, or equivalently, increasing the value of the surface tension gradient and the imposed shear stress on the primary instability induced by the H-mode. Furthermore, a critical value of the Marangoni number is calculated at the inertialess limit, below which the flow is linearly stable. However, the infinitesimal perturbation can be destabilized in this range by including inertia in the flow configuration. If the stability analysis is performed for an inertialess flow over a uniformly heated vertical plane, then the infinitesimal disturbance is always linearly unstable for any nonzero value of the Marangoni number.

However, the numerical solution shows that the thermocapillary S-mode and the thermocapillary P-mode exist along with the H-mode in a low to moderate Reynolds number regime. In particular, the S-mode appears in the low Reynolds number zone, while the P-mode appears in the finite streamwise wave number zone. From the numerical results, we see that the onset of instability for the H-mode decreases, while the onset of stability for the S-mode increases as the imposed shear stress rises. As a consequence, these two onsets merge with each other and generate a single onset of stability for the infinitesimal disturbances at a particular value of the imposed shear stress. By collecting these particular parameter values, we can generate a phase boundary to differentiate the unstable zones for the H-mode and S-mode. In the case of the P-mode, we observe that the unstable zone significantly diminishes with the increasing value of the imposed shear stress, and ultimately vanishes at the higher value of the imposed shear stress. Therefore, one can destabilize the H-mode and the S-mode instabilities but can stabilize the P-mode instability by applying a constant shear stress in the coflow direction. However, if we impose a constant shear stress in the counterflow direction, then the opposite scenario occurs. Furthermore, we see that the H-mode and the S-mode instabilities can be suppressed while the P-mode instability can be intensified by adding the spanwise wave number to the infinitesimal disturbances. This result predicts that the statement of Squire's theorem is not applicable to P-mode instability. Finally, we have noticed that an additional shear mode emerges in the high Reynolds number regime when the inclination angle is sufficiently small. The numerical result demonstrates that the shear mode can be destabilized by imposing a constant shear stress in the coflow direction. By contrast, the shear mode can be stabilized by applying a constant shear stress in the counterflow direction. Furthermore, it is observed that the H-mode and the shear mode compete with each other to dominate the primary instability. The shear mode triggers the primary instability at higher values of the imposed shear stress. As soon as the magnitude of the imposed shear stress is reduced, the H-mode dominates the primary instability. Additionally, we notice that the shear mode can initiate the primary instability if the spanwise wave number is included in the infinitesimal disturbance.

### ACKNOWLEDGMENT

We thank the anonymous referees for their comments and suggestions on improving the manuscript.

**APPENDIX A: SQUIRE'S TRANSFORMATION FOR THE NONISOTHERMAL SHEAR-IMPOSED FLOW**

In this Appendix, we discuss Squire's transformation for the nonisothermal fluid flow in the presence of imposed shear stress. To this end, we use the normal mode solution (42) and write the linearized three-dimensional perturbation equations (31)–(41) in the following forms:

$$ik_x \hat{u} + \partial_y \hat{v} + ik_z \hat{w} = 0, \quad 0 \leq y \leq 1, \quad (\text{A1})$$

$$\text{Re}[(\bar{U} - c)ik_x \hat{u} + \partial_y \bar{U} \hat{v}] = -ik_x \hat{p} + [\partial_{yy} \hat{u} - (k_x^2 + k_z^2) \hat{u}], \quad 0 \leq y \leq 1, \quad (\text{A2})$$

$$\text{Re}(\bar{U} - c)ik_x \hat{v} = -\partial_y \hat{p} + [\partial_{yy} \hat{v} - (k_x^2 + k_z^2) \hat{v}], \quad 0 \leq y \leq 1, \quad (\text{A3})$$

$$\text{Re}(\bar{U} - c)ik_x \hat{w} = -ik_z \hat{p} + [\partial_{yy} \hat{w} - (k_x^2 + k_z^2) \hat{w}], \quad 0 \leq y \leq 1, \quad (\text{A4})$$

$$\text{Pe}[(\bar{U} - c)ik_x \hat{T} + \partial_y \bar{T} \hat{v}] = [\partial_{yy} \hat{T} - (k_x^2 + k_z^2) \hat{T}], \quad 0 \leq y \leq 1, \quad (\text{A5})$$

$$\hat{u} = 0, \quad \hat{v} = 0, \quad \hat{w} = 0, \quad \hat{T} = 0, \quad \text{at } y = 0, \quad (\text{A6})$$

$$\partial_y \hat{u} + ik_x \hat{v} - 2\hat{\eta} = -\text{Ma} \left[ ik_x \hat{T} - \frac{\text{Bi}}{1 + \text{Bi}} ik_x \hat{\eta} \right], \quad \text{at } y = 1, \quad (\text{A7})$$

$$\partial_y \hat{w} + ik_z \hat{v} = -\text{Ma} \left[ ik_z \hat{T} - \frac{\text{Bi}}{1 + \text{Bi}} ik_z \hat{\eta} \right], \quad \text{at } y = 1, \quad (\text{A8})$$

$$-\hat{p} + 2 \cot \theta \hat{\eta} + 2\partial_y \hat{v} - 2ik_x \tau \hat{\eta} = - \left[ \text{We} - \frac{\text{Ma}}{1 + \text{Bi}} \right] (k_x^2 + k_z^2) \hat{\eta}, \quad \text{at } y = 1, \quad (\text{A9})$$

$$\partial_y \hat{T} = \text{Bi} \left[ \frac{\text{Bi}}{1 + \text{Bi}} \hat{\eta} - \hat{T} \right], \quad \text{at } y = 1, \quad (\text{A10})$$

$$(\bar{U} - c)ik_x \hat{\eta} = \hat{v}, \quad \text{at } y = 1. \quad (\text{A11})$$

Next, the following forms of the extended Squire's transformations [36,55] are used:

$$\left. \begin{aligned} k_x \hat{u} + k_z \hat{w} &= k\tilde{u}, & \hat{v} &= \tilde{v}, & k_x^2 + k_z^2 &= k^2, & \hat{p} &= \tilde{p}, \\ c &= \tilde{c}, & k_x \hat{T} &= k\tilde{T}, & k \cot \theta &= k_x \cot \tilde{\theta}, \\ k_x \text{Re} &= k\tilde{\text{Re}}, & k_x \text{Pe} &= k\tilde{\text{Pe}}, & k \text{We} &= k_x \tilde{\text{We}}, \\ k \text{Ma} &= k_x \tilde{\text{Ma}}, & \text{Bi} &= \tilde{\text{Bi}}, & k_x \hat{\eta} &= k\tilde{\eta}. \end{aligned} \right\} \quad (\text{A12})$$

With the help of the above transformations (A12), one can convert the three-dimensional perturbation equations (A1)–(A11) for the nonisothermal film flow into equivalent two-dimensional perturbation equations,

$$ik\tilde{u} + \partial_y \tilde{v} = 0, \quad 0 \leq y \leq 1, \quad (\text{A13})$$

$$\tilde{\text{Re}}[(\bar{U} - \tilde{c})ik\tilde{u} + \partial_y \bar{U} \tilde{v}] = -ik\tilde{p} + [\partial_{yy} \tilde{u} - k^2 \tilde{u}], \quad 0 \leq y \leq 1, \quad (\text{A14})$$

$$\tilde{\text{Re}}[(\bar{U} - \tilde{c})ik\tilde{v}] = -\partial_y \tilde{p} + [\partial_{yy} \tilde{v} - k^2 \tilde{v}], \quad 0 \leq y \leq 1, \quad (\text{A15})$$

$$\tilde{\text{Pe}}[(\bar{U} - \tilde{c})ik\tilde{T} + \partial_y \bar{T} \tilde{v}] = [\partial_{yy} \tilde{T} - k^2 \tilde{T}], \quad 0 \leq y \leq 1, \quad (\text{A16})$$

$$\tilde{u} = 0, \quad \tilde{v} = 0, \quad \tilde{T} = 0, \quad \text{at } y = 0, \quad (\text{A17})$$

$$\partial_y \tilde{u} + ik\tilde{v} - 2\tilde{\eta} = -\tilde{Ma} \left[ ik\tilde{T} - \frac{\tilde{Bi}}{1 + \tilde{Bi}} ik\tilde{\eta} \right], \quad \text{at } y = 1, \quad (\text{A18})$$

$$-\tilde{p} + 2 \cot \tilde{\theta} \tilde{\eta} + 2\partial_y \tilde{v} - 2ik\tau\tilde{\eta} = - \left[ \tilde{We} - \frac{\tilde{Ma}}{1 + \tilde{Bi}} \right] k^2 \tilde{\eta}, \quad \text{at } y = 1, \quad (\text{A19})$$

$$\partial_y \tilde{T} = \tilde{Bi} \left[ \frac{\tilde{Bi}}{1 + \tilde{Bi}} \tilde{\eta} - \tilde{T} \right], \quad \text{at } y = 1, \quad (\text{A20})$$

$$(\tilde{U} - \tilde{c})ik\tilde{\eta} = \tilde{v}, \quad \text{at } y = 1, \quad (\text{A21})$$

where tilde quantities represent the parameters for the two-dimensional nonisothermal shear-imposed film flow. The above transformation shows that  $\tilde{Re} = (k_x/k)Re$ , which indicates that  $\tilde{Re} < Re$ , as  $k_z \neq 0$  for the three-dimensional disturbances. Hence, one can conclude that the primary instability (H-mode instability or shear mode instability) corresponding to the two-dimensional disturbance is linearly more unstable than that of the three-dimensional disturbances for the non-isothermal shear-imposed film flow.

## APPENDIX B: SOLUTION OF THE FIRST-ORDER LONG-WAVE EQUATIONS

$$\phi_1(y) = \frac{y^2}{60} [10(d_0 + d_1 Re) + d_2 y + d_3 y^2 + d_4 y^3], \quad (\text{B1})$$

$$T_1(y) = -\frac{i Bi y}{60(1 + Bi)^3} [e_0 + e_1 y^2 + e_2 y^3 + e_3 y^4], \quad (\text{B2})$$

where

$$d_0 = \frac{3iMa Bi \eta_0}{(1 + Bi)^2} + 6(\eta_1 - i \cot \theta \eta_0),$$

$$d_1 = i(3c_0 - \tau - 2)\eta_0,$$

$$d_2 = 20i \cot \theta \eta_0,$$

$$d_3 = -5iRe c_0 \eta_0,$$

$$d_4 = iRe \eta_0(2 + \tau),$$

$$e_0 = Pe[2Bi\{6Bi - 5(3 + Bi)c_0 + 25\} + 5Bi(4 + Bi)\tau + 20]\eta_0 + 60i Bi(1 + Bi)\eta_1,$$

$$e_1 = 10Bi(1 + Bi)Pe c_0 \eta_0,$$

$$e_2 = -5(1 + Bi)\{1 + Bi(3 + \tau)\}Pe \eta_0,$$

$$e_3 = 3 Bi(1 + Bi)Pe \eta_0.$$

## APPENDIX C: LONG-WAVE SECOND-ORDER APPROXIMATION

The long-wave second-order [ $\mathcal{O}(k^2)$ ] equations are

$$D^4 \phi_2(y) + iRe\{c_0 - \bar{U}(y)\}D^2 \phi_1(y) + (iRe c_1 - 2)D^2 \phi_0(y) + iRe D^2 \bar{U}(y)\phi_1(y) = 0, \quad 0 \leq y \leq 1, \quad (\text{C1})$$

$$D^2 T_2(y) + iPe\{c_0 - \bar{U}(y)\}T_1(y) + (iPe c_1 - 1)T_0(y) + iPe D\bar{T}(y)\phi_1(y) = 0, \quad 0 \leq y \leq 1, \quad (\text{C2})$$

$$\phi_2(y) = 0, \quad T_2(y) = 0, \quad D\phi_2(y) = 0, \quad \text{at } y = 0, \quad (\text{C3})$$

$$D^2 \phi_2(y) + \phi_0(y) + iMa T_1(y) - \frac{iMa Bi \eta_1}{1 + Bi} - 2\eta_2 = 0, \quad \text{at } y = 1, \quad (\text{C4})$$

$$D^3\phi_2(y) + i\text{Re}\{(c_0 - 1 - \tau)D\phi_1(y) + \tau\phi_1\} + (i\text{Re } c_1 - 3)D\phi_0(y) - 2i \cot \theta \eta_1 - 2\tau\eta_0 = 0, \quad \text{at } y = 1, \quad (\text{C5})$$

$$DT_2(y) + \text{Bi} \left[ T_2(y) - \frac{\text{Bi} \eta_2}{1 + \text{Bi}} \right] = 0, \quad \text{at } y = 1, \quad (\text{C6})$$

$$\phi_2(y) - (c_0 - 1 - \tau)\eta_2 - c_1\eta_1 - c_0\eta_0 = 0, \quad \text{at } y = 1. \quad (\text{C7})$$

The coefficients of expression  $c_2$  are

$$\begin{aligned} b_0 &= -80(3 + \tau), & b_1 &= -15\{\text{Ma Pe} + 16(3 + \tau)\}, \\ b_2 &= -720 + 7\text{Ma Pe} + 5(\text{Ma Pe} - 48)\tau, \\ b_3 &= \frac{16\tau - 57}{120(1 + \text{Bi})^2}, & b_4 &= \frac{160 + 49\tau}{252}, \\ b_5 &= \frac{(256 + 77\tau)(\tau + 2)}{1008}. \end{aligned}$$

#### APPENDIX D: EXPRESSIONS OF THE COEFFICIENTS FOR $c_3$

$$h_0 = 6720(1 + \text{Bi})^5[18 \cot \theta - 5\text{We}],$$

$$h_1 = 16800(1 + \text{Bi})[\text{Bi}^2(5 + 3\text{Bi}) - 2],$$

$$h_2 = (1 + \text{Bi})[280\text{Bi}(1 + \text{Bi})(33 - 7\text{Bi}) \cot \theta] + 2100\text{Bi}^2(\text{Bi} - 3),$$

$$h_3 = (1 + \text{Bi})[\text{Bi}\{\text{Bi}(749\text{Bi} + 2090) - 5434\} + 10\text{Bi} \tau \{\text{Bi}(17\text{Bi} + 52)\tau + 254\text{Bi} + 76\text{Bi}^2 - 130\}],$$

$$h_4 = 20(1 + \text{Bi})^4[6617 + 448 \csc^2 \theta + 10\tau(422 + 49\tau)],$$

$$h_5 = \text{Bi}(1 + \text{Bi})[-13720(1 + \text{Bi}) \cot \theta + \text{Pe} \tau(-560\text{Bi} \tau - 3209\text{Bi} + 3490) + (9605 - 3653\text{Bi})\text{Pe}],$$

$$h_6 = 5250\text{Bi}^2,$$

$$h_7 = \frac{2475\text{Bi} \text{Ma}[2\tau(77\tau + 750) + 2707]}{(1 + \text{Bi})^2} - 2 \cot \theta [11\tau(25400\tau + 231519) + 4444928],$$

$$h_8 = (\tau + 2)[13\tau(54800\tau + 434841) + 9711616].$$

#### APPENDIX E: RELATION TO THE SPREADING PROBLEM WHERE THE LIQUID FRONT PROPAGATES IN THE FLOW DIRECTION

To relate our study to the spreading of a viscous film onto a sloping surface [37,38,41], we consider a flow of a two-dimensional incompressible viscous film, where the air flow is blowing across the film surface and produces a constant shear stress  $\tau_s$  in the streamwise direction (see Fig. 14). In fact, the imposed constant shear stress in the present flow configuration behaves like a constant Marangoni surface stress induced by the constant temperature gradient applied to a bounding substrate in the earlier studies [38,41]. Furthermore, we assume that the temperature at the inclined plane is the same as that of the liquid film surface. As a consequence, there is no variation in density, viscosity, and surface tension of the viscous film as the temperature is constant. Within the lubrication approximation ( $\varepsilon = h_c/l_c \ll 1$ , where  $h_c$  and  $l_c$  are, respectively, the characteristic length scales in  $x$  and  $y$  directions, and  $\varepsilon$  is the lubrication parameter), the Navier-Stokes equations and the

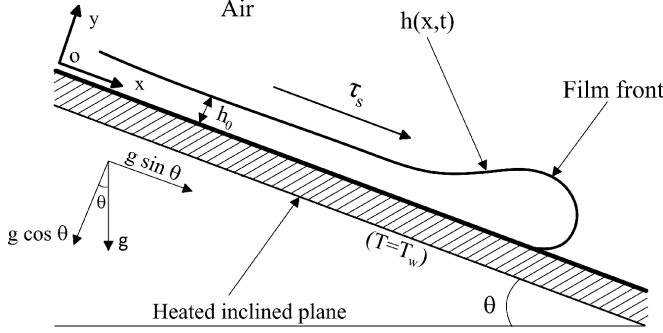


FIG. 14. Sketch of spreading of a viscous film flowing down an inclined plane in the presence of an imposed shear stress in the streamwise direction.

associated boundary conditions are reduced to the following dimensional forms [14,37,38,41]:

$$-\partial_x p + \mu \partial_{yy} u + \rho g \sin \theta = 0, \quad (\text{E1})$$

$$\partial_y p + \rho g \cos \theta = 0, \quad (\text{E2})$$

$$u = 0, \quad \text{at } y = 0, \quad (\text{E3})$$

$$\mu \partial_y u = \tau_s, \quad \text{at } y = h, \quad (\text{E4})$$

$$P_a - p = \sigma \partial_{xx} h, \quad \text{at } y = h, \quad (\text{E5})$$

$$\partial_t h + \partial_x \left( \int_0^h u dy \right) = 0, \quad \text{at } y = h. \quad (\text{E6})$$

It should be noted that the terms  $\rho g \cos \theta$  and  $\sigma \partial_{xx} h$  are kept in the reduced set of equations (E1)–(E6) for small slope angle [ $\varepsilon \cot \theta \sim \mathcal{O}(1)$ ] and for strong curvature near the leading edge of the viscous film [ $\varepsilon^3 \sigma / (\mu U_c) \sim \mathcal{O}(1)$ , where  $U_c$  is the characteristic velocity scale]. Solving the momentum equations (E1) and (E2), we can obtain the height-averaged streamwise velocity of the viscous liquid film,

$$\langle u \rangle = -\frac{h^2}{3\mu} (\rho g \cos \theta \partial_x h - \sigma \partial_{xxx} h - \rho g \sin \theta) + \frac{\tau_s h}{2\mu}. \quad (\text{E7})$$

If the viscous film is very thin, then we can assume  $\rho g \ll \partial_x p$  [39], and consequently, the height-averaged streamwise velocity reduces to

$$\langle u \rangle = \frac{\sigma h^2}{3\mu} \partial_{xxx} h + \frac{\tau_s h}{2\mu}. \quad (\text{E8})$$

The first term in Eq. (E8) represents the contribution of velocity due to surface curvature, while the second term represents the contribution of velocity induced by the surface shear stress. Now if we examine the regime away from the advancing film front (outer regime), the film surface is nearly flat due to negligible surface curvature. Therefore, in this regime, the fluid velocity is dominated by the second term of Eq. (E8) and can be expressed as

$$\langle u \rangle = \frac{\tau_s h}{2\mu}. \quad (\text{E9})$$



Obviously, the imposed surface shear stress and the viscous stress balancing each other in the outer regime and the liquid film spreads with a constant height-averaged velocity  $\frac{\tau_s h_0}{2\mu}$ , where  $h_0$  is the thickness of the flat liquid film. Substituting Eq. (E9) into Eq. (E6), one can obtain the surface evolution equation for the liquid film thickness  $h(x, t)$ ,

$$\partial_t h + (\tau_s/\mu)h\partial_x h = 0. \quad (\text{E10})$$

The above hyperbolic Eq. (E10) is solved by using the method of characteristics, where  $h$  is constant along the characteristic curve given by the equation

$$x = x_0 + (\tau_s/\mu)h(x_0)t, \quad (\text{E11})$$

where  $x_0$  is the initial value of  $x$  at  $t = 0$  when  $h = h(x_0)$ . In what follows, the solution of Eq. (E10) can be written as

$$h(x, t) = [\mu(x - x_0)/(\tau_s t)]. \quad (\text{E12})$$

Therefore, at sufficiently long time and far from the initial location ( $x \gg x_0$ ), the liquid film profile takes a self-similar form,

$$h(x, t) = [(\mu/\tau_s)x/t]. \quad (\text{E13})$$

Now, we will use the global continuity equation [37]

$$\int_0^{x_N(t)} h(x, t)dx = A, \quad (\text{E14})$$

where  $x_N(t)$  is the value of  $x$  at the downstream edge of the outer regime and  $A$  is the cross-sectional area of the viscous film in the  $x$ - $y$  plane. Using the expression of self-similar profile (E13), we can determine the position of the leading edge/downstream edge of the viscous film for the outer regime,

$$x_N = (2A\tau_s/\mu)^{1/2}t^{1/2}. \quad (\text{E15})$$

From Eq. (E13), we can see that the liquid film height increases in the downstream direction from the flat film thickness and achieves its maximum height at the leading edge of the outer regime. Since the film thickness smoothly reduces at a later stage, and finally, meets the impermeable substrate, the capillary force must be significant in this regime (inner regime) along with the viscous stress and the surface shear stress [40]. Hence, both terms of Eq. (E8) are important in the inner regime. Suppose  $l_N$  and  $h_N$  are, respectively, the characteristic length scales in the inner regime in  $x$  and  $y$  directions, where  $h_N$  is the liquid film thickness at the leading edge of the outer regime and  $U_N = \tau_s h_N/(2\mu)$  is the associated height-averaged velocity where  $h = h_N$ . Balancing the two terms of Eq. (E8), we can obtain

$$l_N = (3\text{Ca})^{-1}h_N, \quad (\text{E16})$$

where  $\text{Ca} = \mu U_N/\sigma = \tau_s h_N/(2\sigma)$  is capillary number.

- 
- [1] K. Huang, Y. Hu, and X. Deng, Experimental study on heat and mass transfer of falling liquid films in converging-diverging tubes with water, *Int. J. Heat Mass Transf.* **126**, 721 (2018).  
 [2] P. D. Frisk and E. J. Davis, The enhancement of heat transfer by waves in stratified gas-liquid flow, *Int. J. Heat Mass Transfer* **15**, 1537 (1972).  
 [3] N. Brauner and D. M. Maron, Characteristics of inclined thin films, waviness, and the associated mass transfer, *Int. J. Heat Mass Transfer* **25**, 99 (1982).

- [4] P. L. Kapitza and S. P. Kapitza, Wave flow of thin fluid layers of liquid, *Zh. Eksp. Teor. Fiz.* **19**, 105 (1949).
- [5] T. B. Benjamin, Wave formation in laminar flow down an inclined plane, *J. Fluid Mech.* **2**, 554 (1957).
- [6] C. S. Yih, Stability of liquid flow down an inclined plane, *Phys. Fluids* **6**, 321 (1963).
- [7] S. P. Lin, Instability of a liquid film flowing down an inclined plane, *Phys. Fluids* **10**, 308 (1967).
- [8] G. D. Bruin, Stability of a layer of liquid flowing down an inclined plane, *J. Eng. Math.* **8**, 259 (1974).
- [9] R. Chin, F. Abernathy, and J. Bertschy, Gravity and shear wave stability of free surface flows. Part 1. Numerical calculations, *J. Fluid Mech.* **168**, 501 (1986).
- [10] J. M. Floryan, S. H. Davis, and R. E. Kelly, Instabilities of a liquid film flowing down a slightly inclined plane, *Phys. Fluids* **30**, 983 (1987).
- [11] S. V. Alekseenko, V. Y. Nakoryakov, and B. G. Pokusaev, Wave formation on a vertical falling liquid film, *AIChE J.* **31**, 1446 (1985).
- [12] H. C. Chang, Wave evolution on a falling film, *Annu. Rev. Fluid Mech.* **42**, 1553 (1994).
- [13] J. Liu and J. P. Gollub, Solitary wave dynamics of film flows, *Phys. Fluids* **6**, 1702 (1994).
- [14] A. Oron, S. H. Davis, and S. G. Bankoff, Long-scale evolution of thin films, *Rev. Mod. Phys.* **69**, 931 (1997).
- [15] R. V. Craster and O. K. Matar, Dynamics and stability of thin liquid films, *Rev. Mod. Phys.* **81**, 1131 (2009).
- [16] S. P. Lin, Stability of liquid flow down a heated inclined plane, *Lett. Heat Mass Trans.* **2**, 361 (1975).
- [17] S. Sreenivasan and S. P. Lin, Surface tension driven instability of a liquid film flow down a heated incline, *Int. J. Heat Mass Transfer* **21**, 1517 (1978).
- [18] M. K. Smith, The long-wave instability in heated or cooled inclined liquid layers, *J. Fluid Mech.* **219**, 337 (1990).
- [19] D. Goussis and R. Kelly, On the thermocapillary instabilities in a liquid layer heated from below, *Int. J. Heat Mass Transfer* **33**, 2237 (1990).
- [20] D. A. Goussis and R. E. Kelly, Surface wave and thermocapillary instabilities in a liquid film flow, *J. Fluid Mech.* **223**, 25 (1991).
- [21] S. W. Joo, S. H. Davis, and S. G. Bankoff, Long-wave instabilities of heated falling films: two-dimensional theory of uniform layers, *J. Fluid Mech.* **230**, 117 (1991).
- [22] S. W. Joo, S. H. Davis, and S. G. Bankoff, A mechanism for rivulet formation in heated falling films, *J. Fluid Mech.* **321**, 279 (1996).
- [23] C. Ruyer-Quil, B. Scheid, S. Kalliadasis, M. G. Velarde, and R. K. Zeytounian, Thermocapillary long waves in a liquid film flow. Part 1. Low-dimensional formulation, *J. Fluid Mech.* **538**, 199 (2005).
- [24] B. Scheid, C. Ruyer-Quil, S. Kalliadasis, M. G. Velarde, and R. K. Zeytounian, Thermocapillary long waves in a liquid film flow. Part 2. Linear stability and nonlinear waves, *J. Fluid Mech.* **538**, 223 (2005).
- [25] J. Hu, H. B. Hadid, D. Henry, and A. Mojtabi, Linear temporal and spatiotemporal stability analysis of a binary liquid film flowing down an inclined uniformly heated plate, *J. Fluid Mech.* **599**, 269 (2008).
- [26] J. P. Pascal and S. J. D. D'Alessio, Thermosolutal Marangoni effects on the inclined flow of a binary liquid with variable density. I. Linear stability analysis, *Phys. Rev. Fluids* **1**, 083603 (2016).
- [27] S. J. D. D'Alessio and J. P. Pascal, Thermosolutal Marangoni effects on the inclined flow of a binary liquid with variable density. II. Nonlinear analysis and simulations, *Phys. Rev. Fluids* **1**, 083604 (2016).
- [28] A. Samanta, Stability of inertialess liquid film flowing down a heated inclined plane, *Phys. Lett. A* **372**, 6653 (2008).
- [29] L. A. Dávalos-Orozco, The effect of the thermal conductivity and thickness of the wall on the nonlinear instability of a thin film flowing down an incline, *Int. J. Non Linear Mech.* **47**, 1 (2012).
- [30] L. A. Dávalos-Orozco, Stability of thin liquid films falling down isothermal and nonisothermal walls, *Interfac. Phenom. Heat Transfer* **1**, 93 (2013).
- [31] Z. Ding and T. N. Wong, Falling liquid films on a slippery substrate with Marangoni effects, *Int. J. Heat Mass Transfer* **90**, 689 (2015).
- [32] E. Ellaban, J. P. Pascal, and S. J. D. D'Alessio, Instability of a binary liquid film flowing down a slippery heated plate, *Phys. Fluids* **29**, 092105 (2017).

- [33] U. Thiele, B. Goyeau, and M. G. Velarde, Stability analysis of thin film flow along a heated porous wall, *Phys. Fluids* **21**, 014103 (2009).
- [34] I. M. R. Sadiq, R. Usha, and S. W. Joo, Instabilities in a liquid film flow over an inclined heated porous substrate, *Chem. Eng. Sci.* **65**, 4443 (2010).
- [35] K. A. Ogden, S. J. D. D'Alessio, and J. P. Pascal, Gravity-driven flow over heated, porous, wavy surfaces, *Phys. Fluids* **23**, 122102 (2011).
- [36] A. Choudhury and A. Samanta, Linear stability of a falling film over a heated slippery plane, *Phys. Rev. E* **105**, 065112 (2022).
- [37] H. E. Huppert, Flow and instability of a viscous current down a slope, *Nature* **300**, 427 (1982).
- [38] S. M. Troian, E. Herbolzheimer, S. A. Safran, and J. F. Joanny, Fingering instabilities of driven spreading films, *Europhys. Lett.* **10**, 25 (1989).
- [39] A. M. Cazabat, F. Heslot, S. M. Troian, and P. Carles, Fingering instability of thin spreading films driven by temperature gradients, *Nature* **346**, 824 (1990).
- [40] D. E. Kataoka and S. M. Troian, A theoretical study of instabilities at the advancing front of thermally driven coating films, *J. Colloid Interface Sci.* **192**, 350 (1997).
- [41] V. Ludviksson and E. N. Lightfoot, The dynamics of thin liquid films in the presence of surface-tension gradients, *AIChE J.* **17**, 1166 (1971).
- [42] M. K. Smith, The mechanism for the long-wave instability in thin liquid films, *J. Fluid Mech.* **217**, 469 (1990).
- [43] H. H. Wei, Effect of surfactant on the long-wave instability of a shear-imposed liquid flow down an inclined plane, *Phys. Fluids* **17**, 012103 (2005).
- [44] A. Samanta, Shear-imposed falling film, *J. Fluid Mech.* **753**, 131 (2014).
- [45] F. A. Bhat and A. Samanta, Linear stability analysis of a surfactant-laden shear-imposed falling film, *Phys. Fluids* **31**, 054103 (2019).
- [46] A. Samanta, Spatiotemporal instability of a shear-imposed viscous flow, *Phys. Fluids* **33**, 094104 (2021).
- [47] Y. Y. Trifonov, Counter-current gas-liquid wavy film flow between the vertical plates analyzed using the Navier-Stokes equations, *AIChE J.* **56**, 1975 (2010).
- [48] Y. Y. Trifonov, Instabilities of a gas liquid flow between two inclined plates analyzed using the Navier-Stokes equations, *Int. J. Multiphase Flow* **95**, 144 (2017).
- [49] O. Y. Tselodub and A. A. Bocharov, Modeling nonlinear wave regimes in a falling liquid film entrained by a gas flow, *Chaos, Solitons Fractals* **104**, 580 (2017).
- [50] O. Y. Tselodub and A. A. Bocharov, Simulating solitary waves on a flowing down liquid film entrained by a gas stream, *Eur. J. Mech. B Fluids* **72**, 449 (2018).
- [51] S. Kalliadasis, C. Ruyer-Quil, B. Scheid, and M. G. Velarde, *Falling Liquid Films* (Springer, Berlin, 2012).
- [52] S. Miladinova, S. Slavtchev, G. Lebon, and J. C. Legros, Long-wave instabilities of non-uniformly heated falling films, *J. Fluid Mech.* **453**, 153 (2002).
- [53] A. Samanta, Stability of liquid film falling down a vertical non-uniformly heated wall, *Physica D* **237**, 2587 (2008).
- [54] A. Samanta, Optimal disturbance growth in shear-imposed falling film, *AIChE J.* **66**, e16906 (2020).
- [55] A. Samanta, Modal analysis of a viscous fluid falling over a compliant wall, *Proc. Roy. Soc. A* **477**, 20210487 (2021).
- [56] S. Kalliadasis, E. A. Demekhin, C. Ruyer-Quil, and M. G. Velarde, Thermocapillary instability and wave formation on a film falling down a uniformly heated plane, *J. Fluid Mech.* **492**, 303 (2003).
- [57] A. Samanta, Linear stability of a plane Couette-Poiseuille flow overlying a porous layer, *Int. J. Multiphase Flow* **123**, 103160 (2020).
- [58] A. Samanta, Modal and nonmodal stability analysis for an electrified falling film, *Phys. Rev. E* **107**, 045105 (2023).
- [59] A. Samanta, Spatiotemporal instability of an electrified falling film, *Phys. Rev. E* **93**, 013125 (2016).
- [60] P. G. Drazin and W. H. Reid, *Hydrodynamic Stability* (Cambridge University Press, Cambridge, UK, 1981).
- [61] P. M. J. Trevelyan and S. Kalliadasis, Wave dynamics on a thin-liquid film falling down a heated wall, *J. Eng. Math.* **50**, 177 (2004).

- [62] U. Lange, K. Nandakumar, and H. Raszillier, Symbolic computation as a tool for high-order long-wave stability analysis of thin film flows with coupled transport processes, *J. Comput. Phys.* **150**, 1 (1999).
- [63] S. Pal and A. Samanta, Linear stability of a surfactant-laden viscoelastic liquid flowing down a slippery inclined plane, *Phys. Fluids* **33**, 054101 (2021).
- [64] P. Schmid and D. Henningson, *Stability and Transition in Shear Flows* (Springer, Berlin, 2001).
- [65] R. E. Kelly, D. A. Goussis, S. P. Lin, and F. K. Hsu, The mechanism for surface wave instability in film flow down an inclined plane, *Phys. Fluids A* **1**, 819 (1989).
- [66] N. Tilton and L. Cortelezzi, Linear stability analysis of pressure-driven flows in channels with porous walls, *J. Fluid Mech.* **604**, 411 (2008).
- [67] A. Samanta, Role of slip on the linear stability of a liquid flow through a porous channel, *Phys. Fluids* **29**, 094103 (2017).
- [68] A. Samanta, Shear wave instability for electrified falling films, *Phys. Rev. E* **88**, 053002 (2013).
- [69] F. A. Bhat and A. Samanta, Linear stability of a contaminated fluid flow down a slippery inclined plane, *Phys. Rev. E* **98**, 033108 (2018).
- [70] L. N. Howard, Note on a paper of John W. Miles, *J. Fluid Mech.* **10**, 509 (1961).